Automated Three-Dimensional Identification and Tracking of Micro/Nanobiological Organisms by Computational Holographic Microscopy

An optical system can automatically identify a biological organisms from a digital holographic image and then recognize the identified organism in other holographic images.

By Inkyu Moon, Mehdi Daneshpanah, Bahram Javidi, *Fellow IEEE*, and Adrian Stern

ABSTRACT | The ability to sense, track, identify, and monitor biological micro/nanoorganisms in a real-time, automated, and integrated system is of great importance from both scientific and technological standpoints. Such a system and its possible variants would have numerous applications in a wide spectrum of fields, including defense against biological warfare, disease control, environmental health and safety, and medical treatments. In this paper, we review a comprehensive mixture of optical and computational tools developed in our group aiming at real-time sensing and recognition of biological microorganisms. Digital in-line holographic microscopy is used with both coherent and partially coherent illumination to probe the specimen interferometerically. The interference pattern is then recorded on an optoelectronic image sensor and transferred to a computer where special statistical algorithms are performed to segment, recognize, and track the microorganisms within the field of view of the microscope. The advantages of proposed holographic sensing are described compared to conventional two-dimensional imaging systems. In addition, the theoretical aspects and fundamental limitations of digital in-line holographic microscopy are discussed, which determine the relationship between system parameters and achievable performance. The proposed optical-digital integrated system for automated, real-time sensing and recognition of biological microorganisms has been deemed promising with the potential of widespread application. We demonstrate how the proposed techniques function together in a series of experiments.

KEYWORDS | Biophotonics; Gabor feature extraction; holographic microscopy; noninvasive biosensing; three-dimensional image recognition; three-dimensional image segmentation and tracking; three-dimensional optical imaging

I. INTRODUCTION

Real-time automated identification of pathogenic micro/nanobiological organisms or other specimen has many potential applications in security and defense or health-related applications. Therefore, developing reliable, automated, and low-cost methods for real-time sensing, monitoring, and identification of harmful pathogens or malignant cells are beneficial in combating catastrophic pandemics, disease detection, and monitoring for emerging

medical treatment procedures, food safety, environmental health and safety monitoring, etc. Conventional methods used to inspect and identify bacteria and other biological species often involve labor-intensive and time-consuming biochemical and/or biomolecular processing.

Optical imaging systems based on digital holography have been extensively investigated for three-dimensional (3-D) visualization and recognition of rigid, macro objects [1]–[22]. However, biological organisms are typically nonrigid and exhibit dynamic behavior such as moving, dividing, and growing. Such dynamic nature makes it difficult to identify biological species based on their shape, size, or morphology in conventional (2-D) imaging. Moreover, many unicellular biological species such as bacteria, yeast, or protozoans appear essentially transparent under bright field microscope unless the specimen is stained and/or fixed; a process in which the cells are killed and dynamics cannot be studied. Meanwhile, 2-D intensity images of the microorganisms are usually insufficient for identification or visualization of transparent microorganism parts, e.g., sperm tails. The approach that we provide an overview of in this paper relies on interferemetric complex amplitude wavefront sensing and statistical analysis of the data. The light that passes through the specimen interacts with intricate structures within the microorganism, changing the amplitude and phase of the exiting wavefront. In microorganisms, the absorption of visible light by cytoplasmic material (lipids, proteins, water) is usually not prominent; nevertheless, the refractive index variation inside the microorganisms affects the phase of the exiting wavefront more dramatically. Thus, the phase of the wavefront may carry more information about the specimen compared with its amplitude. Among the techniques investigated for real-time micro/nanobiological organism identification, we provide an overview of in-line digital holographic microscopy because it facilitates acquisition of both scalar components of the wavefront, i.e., amplitude and phase, in an interferometeric setting that provides 3-D information about the specimen [23]–[27]. In in-line digital holographic microscopy, the phase information associated with biological micro/nanoorganisms is recorded interferometerically, allowing for the study of semitransparent biological specimen that would otherwise die from staining or may appear in low contrast or nearly invisible under bright field microscopy techniques.
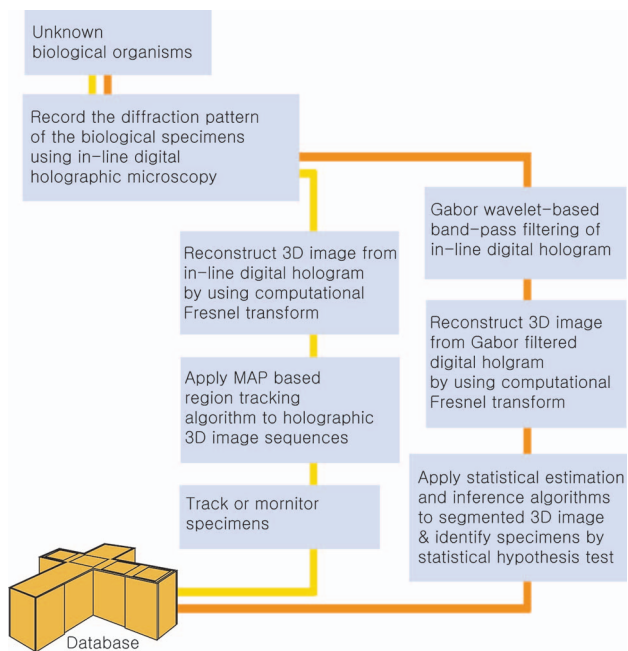
This paper reviews the optical systems and computational algorithms for automated, optimal 3-D identification and tracking of micro/nanobiological organisms using in-line digital holographic microscopy. In this approach, an in-line digital holographic setup enables real-time sensing and 3-D visualization of specimen. Unlike phase-shifting digital holography [2], this technique is suitable for studying the dynamics of the biological specimen since it only requires a single exposure of the imaging sensor to record the dif-

fraction pattern of the specimen. Also, in contrast to conventional 3-D microscopy methods, such as laser scanning confocal or multiphoton excitation, which require mechanical scanning of the beam in the transverse plane and mechanical translation along the optical axis to bring the cells in focus, the method described here makes it possible to automatically reconstruct the focused images of each individual microorganism in the field of view computationally from a single recoded digital hologram. In addition, there is no need for the specimen to be stained or fixed in this method. Thus, living biological specimen can be studied in their most undisturbed state, noninvasively. We present experiments to demonstrate real-time 3-D sensing, identification, and tracking of real biological microorganisms owing to the fact that an in-line digital hologram of the specimen contains the information about the diffracted field by the specimen in 3-D. Also, unlike other multiexposure interferometry methods, the single-exposure in-line holographic microscopy gets around extreme sensitivity to the environmental noise and thus provides a robust wavefront sensing alternative suitable for field applications.

To acquire the phase information of biological specimen, the sample is illuminated with coherent light and the diffracted light from the specimen is collected and magnified optically through a microscope objective and recorded on a charge-coupled device (CCD) sensor array interfaced with a computer. Next, the magnified 3-D reconstruction, i.e., stack of 2-D complex optical fields diffracted by the specimen, is numerically reconstructed from the single in-line digital hologram using the Huygens–Fresnel integral equation. Such computational reconstruction allows for analyzing the electric field variation in the longitudinal dimension as well as the transverse plane. Such multiplane reconstruction capability allows the phase distributions, which may be ambiguous in one plane, to be uniquely identified when the wavefront propagation is observed across multiple planes.

Fig. 1 depicts the flowchart of the 3-D holographic sensing, identification, and tracking system reviewed in this paper. In the first stage of the process, an in-line digital holographic microscope records the optical diffraction pattern of the unknown micro/nano biological organism using a microscope objective and CCD [23], [24]. The Gabor wavelet filtering is then applied to the recorded hologram to extract specific identifying features from the interference patterns of biological specimen by decomposing the patterns in the spatial frequency domain for optimal identification purposes. After preprocessing and conditioning the recorded digital hologram, Fresnel transformation is applied to reconstruct the multiscale and multiresolution complex-valued image of the biological specimen at an arbitrary depth along the optical axis [25]–[27].

Next, special statistical algorithms for segmentation of complex-valued hologram reconstruction images are used to isolate the regions that microorganisms reside and to

Unknown
biological organisms

Record the diffraction pattern
of the biological specimens
using in-line digital
holographic microscopy

Reconstruct 3D image from
in-line digital hologram
by using computational
Fresnel transform

Apply MAP based
region tracking
algorithm to holographic
3D image sequences

Track or mornitor
specimens

Gabor wavelet–based
band–pass filtering of
in–line digital hologram

Reconstruct 3D image
from Gabor filtered
digital holgram
by using computational
Fresnel transform

Apply statistical estimation
and inference algorithms
to segmented 3D image
& identify specimens by
statistical hypothesis test

Database

Fig. 1. *Block diagram for automated three-dimensional identification and tracking of micro/nanobiological organisms by in-line digital holographic microscopy.*

ignore the background solution [28]. We utilize a bivariate jointly Gaussian distribution model for amplitude and phase to represent complex-valued hologram reconstruction data. Such modeling allows us to take into account the correlation between the amplitude and phase of the reconstructed wavefront. The segmentation of microorganisms is performed using a polygonal representation (snake) for the microorganism boundary accompanied by a stochastic optimization of a maximum likelihood based metric [28].

Moreover, the ability to track the microorganisms is helpful in their recognition as well as time lapse study of their behavior. We overview 3-D tracking algorithms based on maximum *a posteriori* (MAP) tracker tailored for digital hologram sequences [29]. In this approach, the microorganism surface is modeled as the isosurface of a level set function, which is evolved at each new hologram frame via level set Hamilton–Jacobian update rule. The statistical characteristics of the target microorganism versus the background are exploited to evolve the interface at each new frame; thus the algorithm works independent of the shape or morphology of the target. The tracker is initialized with the results of the segmentation process and tracks the movement of microorganisms in each hologram frame. The regions tagged for presence of microorganisms will then be used for recognition purposes.

For 3-D recognition, the empirical cumulative density function is calculated from the segmented regions, which are obtained from the multiscale, multiresolution complex

images using segmentation and tracking steps discussed above. Then, statistical hypothesis testing is performed to compare the unknown biological specimen under investigation against the training sets in the reference database. The result of the hypothesis testing determines the classification of the microorganism with a specific p-value [27]. The strength of the reviewed methods for identification and recognition owes to the new information that holographic sensing provides in form of complex amplitude wavefront reconstructions at arbitrary depths. This information offers more discriminating features for recognition of biological species compared to 2-D intensity images.

This paper is organized as follows. In Section II, we overview principles of in-line digital holographic microscopy. The theoretical analysis on fundamental limits of this technique and the influence of the conjugate image on the visualization and recognition performance are investigated in Section III. Segmentation algorithm for complex valued hologram reconstructions is reviewed in Section IV. Three-dimensional recognition by using Gabor filtered hologram and a statistical classifier are described in Section V. In Section VI, 3-D tracking algorithm is described. In Section VII, experimental results are demonstrated. Multidimensional imaging and identification of biological microorganisms is briefly discussed in Section VIII. The conclusions follow in Section IX.

II. SINGLE EXPOSURE IN-LINE DIGITAL HOLOGRAPHIC MICROSCOPY

The in-line digital hologram of biological specimen is recorded on an image sensor array as shown in Fig. 2 [24]–[29]. An argon laser with center wavelength of 514.5 nm is used to provide spatially and temporally coherent illumination. The planar coherent wavefront illuminates the biological specimen and the microscope objective captures and magnifies the transmitted diffracted wavefront to form an image on the hologram plane. Since biological organisms are semitransparent, a fraction of the incident light passes through without getting diffracted by means of ballistic photons, which provides a reference beam for interferometry. The image sensor array at the location of the hologram plane captures the interference of the reference wave and the diffracted wavefronts from the biological specimen. The resulting intensity fringe patterns contain both the magnitude and phase information of the biological specimen.

The system requires only a single exposure to record a hologram of the specimen. Therefore, in-line digital holographic microscopy is suitable for studying dynamic events such as moving, growing, or dividing of biological specimen. Also, the system is robust to external noise factors, such as platform vibration, since multiple exposures are not required as in the phase-shift interferometry technique [2]. If a separate reference beam is not
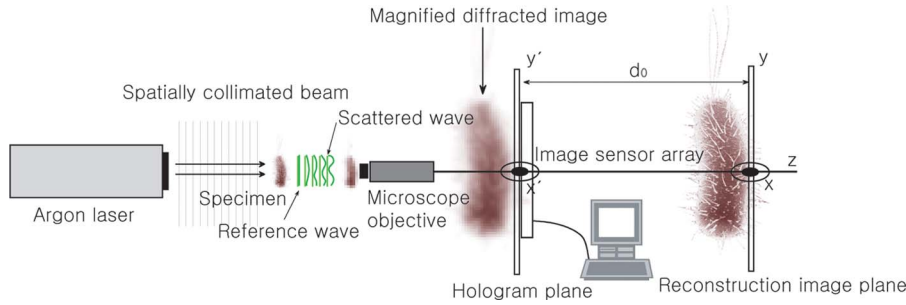
Fig. 2. *A schematic of the in-line digital holography setup for 3-D sensing, recording, and reconstruction of micro/nanobiological organisms.*

used, the in-line digital holographic microscope system is analogous to digital implementation of the Gabor hologram [30], where the diffracted optical field from the specimen is reconstructed by digital algorithms.

The interference between diffracted (object) and undiffracted (reference) wavefronts creates the intensity pattern

$$
\begin{aligned}
I(x', y', z') = I(\vec{r}) &= \left| A e^{j(\vec{k}_o \cdot \vec{r})} + a e^{j(\vec{k}_r \cdot \vec{r})} \right|^2 \\
&= |A|^2 + |a|^2 + 2|A||a| \\
&\quad \times \cos\left[(\vec{k}_r - \vec{k}_o) \bullet \vec{r} + \phi_i \right]
\end{aligned} \quad (1)
$$

where $|A|^2$ and $|a|^2$ are the object and reference beam intensities, respectively. $\vec{k}_r$ and $\vec{k}_o$ are wave vectors of reference and object waves, respectively, and $\vec{r}$ is the position vector. According to diffraction theory, the field distribution at the reconstructed image plane can be written as [5]

$$
\begin{aligned}
O(x, y, z)_{d_0 \leq z \leq d_r} = \frac{z}{j\lambda} \iint &\left\{ I(x', y', z' = 0) \right. \\
&\left. \times \frac{e^{j\frac{2\pi}{\lambda}\left(\sqrt{z^2 + (x-x')^2 + (y-y')^2}\right)}}{z^2 + (x-x')^2 + (y-y')^2} \right\} dx'dy'
\end{aligned} \quad (2)
$$

where $I(x', y', z' = 0)$ is the interference pattern of the biological specimen recorded at the image sensor plane (see Fig. 2), d_0 is the distance between the focused reconstruction plane and recording plane, and d_r is an arbitrary depth between the recording plane and the reconstruction image plane along the z-axis. The function $O(x, y, z)$ enables one to obtain 3-D information of the transfiguration of the wavefront exiting a biological specimen. Wavefronts at arbitrary depth along the z-axis, including the one representing the microorganism in focus, are computed from a single in-line digital hologram.

For the numerical 3-D reconstruction, (2) can be simplified and evaluated by applying a binominal approximation to the Huygens–Fresnel principle integral as follows:

$$
\begin{aligned}
&O(x, y, z)_{d_0 \leq z \leq d_r} \\
&= \iint \left\{ \frac{e^{j2\pi z/\lambda}}{j\lambda z} e^{j\frac{\pi}{\lambda z}(x^2 + y^2)} I(x', y', z' = 0) \right. \\
&\qquad \left. \times e^{j\frac{\pi}{\lambda z}(x'^2 + y'^2)} e^{-j\frac{2\pi}{\lambda z}(xx' + yy')} \right\} dx'dy' \\
&= \frac{e^{j\frac{2\pi}{\lambda}z}}{j\lambda z} \left\{ I(x', y', z' = 0) \otimes e^{j\frac{\pi}{\lambda z}(x^2 + y^2)} \right\}
\end{aligned} \quad (3)
$$

where $\otimes$ is the convolution operator. In other words, (3) represents the Fresnel transformation (FrT) of the recorded intensity at distance z along the z-axis.

Use of partially coherent light with short coherence length has also been investigated for digital holography [6], [25]. In this paper, we provide an overview of the use of such sensing apparatus for 3-D visualization and identification of biological microorganisms using statistical pattern recognition techniques. Fig. 3 shows a schematic diagram of digital holographic microscopy with partially coherent illumination for holographic recording and 3-D reconstruction of biological specimen [25]. In our implementation, a Xenon lamp radiation is bandpass filtered, centered at 520 nm with a bandwidth of 10 nm, and is subsequently spatially filtered and collimated to illuminate the specimen under investigation. The short coherence length associated with the large bandwidth of the filtered light is not problematic since the reference wave travels the same path as the object wave, as shown in Fig. 3. In fact, the illuminating beam is partially diffracted by the sample, and meanwhile a fraction of the beam passes through without diffraction (as ballistic photons), which forms the desired reference wavefront. As in the coherent case, the exiting wavefront is magnified by a microscope objective onto the hologram plane. Plane by
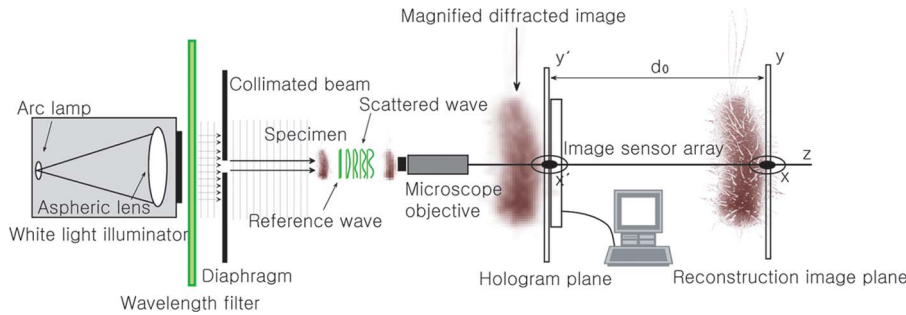
Fig. 3. *A schematic of the partially coherent digital holography setup for the 3-D sensing, recording, and reconstruction of micro/nanobiological organisms.*

plane visualization of the specimen is performed by applying the Fresnel transform on the intensity of the diffraction pattern as described in (3) with the center wavelength of the filter used for λ.

There are merits in using partially coherent illumination for holographic sensing. First is the reduction of unwanted noise such as speckle and interference from multiple reflections off of optical surfaces. The second benefit is in the wide spectrum of the light that can be used to interrogate the specimen to obtain 3-D spectral information.

III. RESOLUTION AND FIELD OF VIEW (FOV) LIMITATIONS IN IN-LINE DIGITAL HOLOGRAPHIC MICROSCOPY

The resolution and field of view (FOV) of the digital holographic microscopy are primarily limited by the digital recording sensor (typically a CCD). The signal captured by the CCD is integrated within the area of each pixel element (with size Δ), sampled along the pixel array and also spatially limited by the CCD size (W_s). It can be shown that if the object field *maximum local bandwidth* (MLB) [31], [32] is smaller than $1/\Delta$, then the aliasing problem can be alleviated by proper postprocessing [31], [33]. We can summarize the three spatial spatial-frequency limitations set by the sensor as [34]

$$W_H \leq W_s \text{ and } B_H \leq B_s = (\alpha\Delta)^{-1} \text{ and } MLB \leq \Delta^{-1} \quad (4)$$

where $\alpha \in (0,1)$ is the pixel fill factor and W_H and B_H are the width and (double sided) bandwidth of the object complex field amplitude at the hologram plane, respectively. We note that besides the above-described resolution and FOV limitations set by the pixilated sensor, further limitations may be induced by the microscope objective that will be considered later in this section.

The Wigner domain is particularly useful for holography exploration [35]. The object complex field amplitude $u_0(x)$ can be represented uniquely in the space-frequency domain by applying the Wigner–Ville transform (WVD) as [32], [33], [35]

$$W_{u_0}(x,\nu) = \int\limits_{-\infty}^{\infty} u_0\left(x + \frac{x'}{2}\right)u_0^*\left(x - \frac{x'}{2}\right)$$
$$\times \exp(-j2\pi x'\nu)dx' \quad (5)$$

where ν denotes the spatial frequency. The WVD describes the local space-frequency distribution (phase-space distribution) of the optical fields involved in the holographic process. For example, let us consider an object with width W_0 and essential bandwidth B_0. Its support in the WVD domain is a rectangle as shown in Fig. 4(a). As the object field propagates through the system, its Wigner distribution changes as described, for example, in Fig. 4(b) for the special case of free-space propagation. One can use the WVD as a tool to analyze the behavior of the digital holographic microscope system.

To achieve a better resolution for microscopic applications, optical magnification should be employed using an objective lens, i.e., to record a hologram in the image plane of the objective lens. Let us assume that imaging condition $1/z_1 + 1/z_2 = 1/f$ is fulfilled, where f is the lens focal distance, z_1 is object distance to the lens, and z_2 is the image plane distance from the lens. It can be shown [35] that the support in the WVD domain of the field $u_i(x)$ in the image plane is

$$W_{u_i}(x,\nu) = W_{u_0}\left(-\frac{x}{M}, -M\nu - \frac{x}{\lambda f M}\right) \quad (6)$$

where $M = z_2/z_1$ is the absolute lateral magnification. In deriving (6) it is assumed that the lens aperture is sufficiently
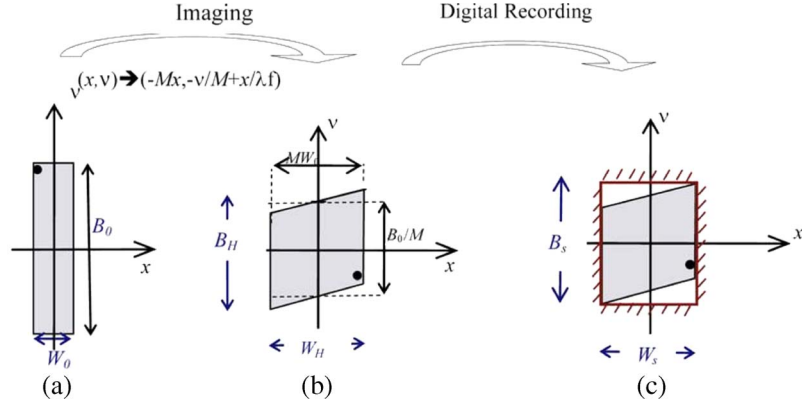
Fig. 4. *(a) The Wigner chart of the original field, (b) the field in the image plane, and (c) together with the sensor limitations.*

large so that the image is not diffraction limited. The effect of the aperture lens will be considered later. The corresponding Wigner chart is shown in Fig. 4(b). It can be seen that the object size is increased by M, so that $W_H = MW_0$. Therefore, since for lossless recording W_H should not exceed W_s, the object size needs to fulfill

$$W_0 = \frac{W_H}{M} \leq \frac{W_s}{M}. \tag{7}$$

From geometrical considerations in Fig. 4(a) and (b), together with (7), we find the overall bandwidth of the field at the sensor plane to be $B_H = (B_0/M) + (W_0/\lambda f)$ [36]. This, together with the second condition in (4), yields

$$B_0 \leq \frac{M}{\alpha \Delta} - \frac{MW_0}{\lambda f}. \tag{8}$$

In addition, we need to fulfill the sampling condition, i.e., $W_0 \leq W_s - \lambda z B_0$, $W_0 \leq \lambda z/\Delta$. Noticing that $MLB = B_0/M$, the third condition in (4) yields

$$\frac{B_0}{M} \leq \frac{1}{\Delta}. \tag{9}$$

In the above discussion, we assume that the objective lens aperture is virtually infinite. Objective with aperture A acts as a low-pass filter with cutoff spatial frequency $A/\lambda z_2$ in the image plane coordinates [37] or, equivalently, $A/\lambda z_1$ in the object plane coordinates. Consequently, finite aperture simply imposes an additional limitation on the object bandwidth

$$B_0 \leq 2\nu_c = 2A/\lambda z_1. \tag{10}$$

Thus, we may summarize the three conditions on the object bandwidth as

$$\begin{aligned} B_0 &\leq \min\left(\frac{M}{\Delta}, \frac{M}{\alpha\Delta} - \frac{W_0}{\lambda f}, \frac{2A}{\lambda z_1}\right) \\ &= \frac{M}{\Delta}\min\left(1, \frac{1}{\alpha} - \frac{W_0\Delta}{\lambda f}, \frac{2A\Delta}{\lambda z_1 M}\right). \end{aligned} \tag{11}$$

Note that with proper magnification M, imaging holography permits capturing higher bandwidth than Fresnel holography. If we are interested to visualize object details of size δ, so that $B_0 \cong 1/\delta$, and assuming that the system is not diffraction limited (that is, $B_0 = M/\Delta \leq 2A/\lambda z_1$ or, equivalently, $1/\Delta \leq 2A/\lambda z_2$), then, according to (11), the required magnification is

$$M \geq \frac{\Delta}{\delta \min(1, 1/\alpha - \Delta W_0/(\lambda f))}. \tag{12}$$

As can be seen in Fig. 4(c), with image plane holography, the sensor recording capacity is not fully utilized, and there is an overhead of $MW_0^2/\lambda f$ in the space-bandwidth product depending on the propagation distance [36].

Now, we will investigate the conditions for which the conjugate term in the in-line digital hologram in (1) is negligible, thus allowing an almost precise object reconstruction. The single exposure in-line hologram formation and reconstruction can be easily understood from examining the Wigner space of the optical fields involved shown in Fig. 5. Fig. 5(a) shows the Wigner chart of the field u_i in the objective image plane. The width W_i and bandwidth B_i of the field u_i in the image plane of the objective are the same as those found earlier as $W_i = MW_0$ and $B_i = (B_0/M) + (W_0/\lambda f)$, respectively [see Fig. 4(b)]. The free propagation of u_i over the distance d is represented by an x-shearing of the Wigner domain, in a similar way as
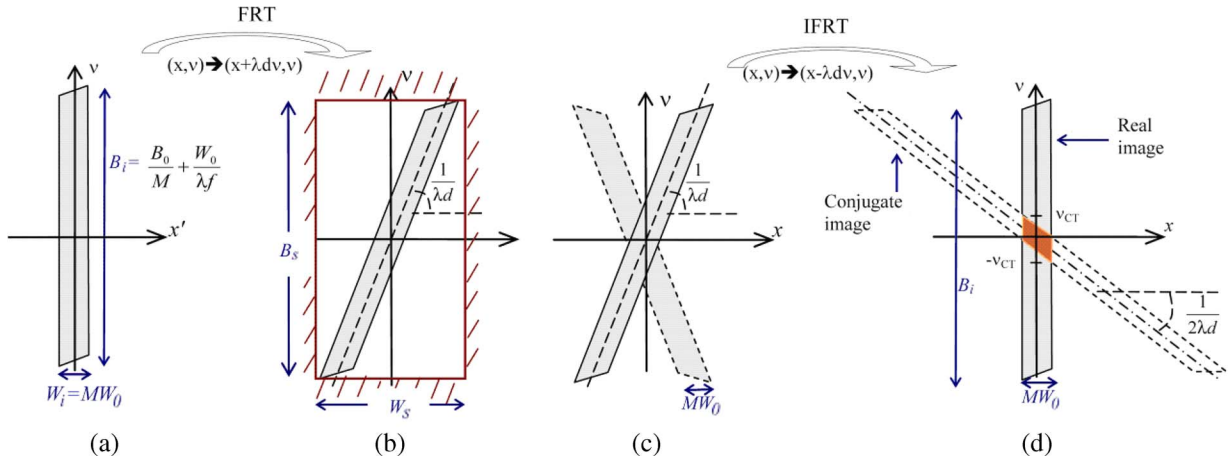
Fig. 5. *Support of the Wigner chart of the (a) field u_i in the image sensor (CCD) plane, (b) field u_h in the CCD plane, (c) field u_h and its conjugate u_h^* extracted from the recorded field, and (d) reconstructed fields using inverse Fresnel transform.*

in Fig. 4(b). The appropriate Wigner chart of the object field u_h at the CCD plane is shown in Fig. 5(b). Free-space propagation, represented mathematically by the Fresnel transform, preserves the bandwidth; therefore the bandwidth of u_h remains the same as that of u_i as $B_h = (B_0/M) + (W_0/\lambda f)$. However, the width of the field is spread due the free-space propagation. One can find the width of u_h to be $W_h = W_i + \lambda dB_i = MW_0 + \lambda d((B_0/M) + (W_0/\lambda f))$ and MLB$= W_i/\lambda d = MW_0/\lambda d$. Here, d is the distance between the objective image plane and the CCD camera and MLB is the maximum local bandwidth. Thus, we may summarize the three spatial-frequency limitations set by the sensor as follows:

$$MW_0 + \lambda d\left(\frac{B_0}{M} + \frac{W_0}{\lambda f}\right) \le W_s, \quad \frac{B_0}{M} + \frac{W_0}{\lambda f} < \frac{1}{\alpha\Delta}$$
$$\frac{MW_0}{\lambda d} < \frac{1}{\Delta}. \tag{13}$$

In in-line digital holographic microscopy, in addition to the above-described limitations set by the CCD sensor, we have to consider also reconstruction constrains due the fact that only one exposure is processed. Fig. 5(c) and (d) illustrates the reconstruction process. Since the CCD captures intensities, the captured hologram consists of the object field u_h together with its conjugate image u_h^*. By applying an inverse Fresnel transform, the Wigner chart is sheared in an opposite direction to the shearing caused by the direct Fresnel transform. The resulting Wigner chart is depicted in Fig. 5(d). It can be seen that in the range $-MB_0/2 < x < MB_0/2$, the Wigner chart of the reconstructed filed is very similar to that of u_i in Fig. 5(a). The conjugate field interferes with the object

field only in the range $-\nu_{CT} < \nu < \nu_{CT}$, where ν_{CT} is given by [34]

$$\nu_{CT} = \frac{MB_x}{2\lambda d}. \tag{14}$$

A figure of merit accounting for the crosstalk noise distortion in the reconstructed image can be defined by the ratio of the object Wigner chart and that of the conjugate filed within the reconstruction interval $\left(-MW_0/2 < x < MW_0/2\right)$

$$\mathrm{SCR} = \frac{B_i}{MB_x/2\lambda d} = \frac{\frac{B_0}{M} + \frac{W_0}{\lambda f}}{MB_x/2\lambda d}. \tag{15}$$

From (15), we see that the crosstalk between the conjugate image to the real image is inversely proportional to approximately M^2. This implies that better reconstructions are obtained with the smallest M allowed by conditions in (13), which in most practical cases is dominated mainly by $(B_0/M) + (W_0/\lambda f) < 1/\alpha\Delta$ and is on the order of $(1/B_0)/\lambda f$.

IV. SEGMENTATION OF BIOLOGICAL MICROORGANISMS IN RECONSTRUCTED DIGITAL HOLOGRAMS

A critical step for recognition of different species is the segmentation of reconstructed images from in-line digital holograms to isolate the regions within the FOV in which microorganisms reside while ignoring the rest of the

background. In this section, we review a method described in [28] for segmentation of complex reconstructed digital holograms of microorganisms using the bivariate jointly distributed region snake method. This technique is based on a statistical framework capable of handling complex valued reconstructed digital holograms by using the joint probability distribution of magnitude and phase information of the diffracted optical field by the specimen. An optimization criterion is derived by maximizing the likelihood function of the target (microorganism) support hypothesis $H_{\mathbf{w}}$, while no knowledge of the statistical properties of the target or background is assumed known a priori. Instead, a maximum likelihood estimator estimates the necessary statistical parameters.

Moreover, target and background pixels are assumed to have independent bivariate Gaussian distribution for their magnitude and phase contents, respectively. The interference pattern recorded on the hologram plane contains a relatively large dc component due to the in-line design of the microscope. Thus, as a result of FrT [see (3)], the imaginary part of the reconstructed optical field is small compared to the real part. Consequently, the phase distribution that would otherwise be uniform between zero and 2π is squeezed in a smaller range and shows a bell-shaped distribution that closely resembles a Gaussian distribution. The choice of Gaussian distribution model for phase is based upon several experimental observations and matches closely with collected data.

The proposed method uses the concept of snake active contours [28], [38]–[40] for separating the target from the background scene by a target support hypothesis $H_{\mathbf{w}}$. A snake is essentially a closed contour that can be approximated by a multinode polygon, which evolves during the segmentation process to minimize a certain criterion known as the snake energy [40]. This contour divides the image into inner and outer regions, which are denoted by Ω_{tar} (target) and Ω_{bck} (background), respectively. A stochastic algorithm is utilized to carry out the optimization and guide the deformations of the snake to eventually force the snake contour to converge to the actual microorganism boundary.

There are several advantages for using the bivariate jointly distributed region snake algorithm [28], [38], [39]. In fact, the bivariate joint distribution of magnitude and phase information provides a more accurate data model for the reconstructed images of in-line digital holography, since it captures the correlation between each pixel's magnitude and phase content. This is due to the fact that the intracellular structures and organelles that absorb light more efficiently usually have higher density of macromolecules, such as protein and lipids, compared to cytosol, which is mainly constituted from hydrophilic molecules. That is in contrast with independent distribution analysis, which treats the magnitude and phase information as independent random variables and consequently ignores the correlation of these two correlated random variables. In fact, the computed cross-correlation between magnitude and phase at each reconstructed plane in our experiments is approximately 0.3, which verifies this argument. In addition, in the region snake regime, the evolution of the snake contour is not dependent of local pixels near the contour edge as in classic snake active contours [40], but rather, the evolution process is based on the statistical distribution of the information inside and outside the snake contour. The latter fact facilitates segmentation of objects even when they are out of focus or images with jagged object boundaries.

Since the reconstructed hologram images are complex-valued, polar representation is used for its pixels as $s_i = \alpha_i \exp(j\varphi_i)$, with α_i and φ_i denoting the magnitude and phase, respectively. The target and background pixels are assumed to follow two independent bivariate Gaussian distributions. Each distribution has a probability density function that consists of two dependent Gaussian random variables α and φ for magnitude and phase, respectively. The original bivariate Gaussian probability density function is not separable directly. However, by conditioning one of the variables α on the second variable φ, one can obtain the separated form of bivariate Gaussian probability distribution function as follows [41]:

$$f_\ell(\alpha_i, \varphi_i) = \frac{1}{\sigma_\varphi^\ell} \Phi\left(\frac{\varphi_i - \mu_\varphi^\ell}{\sigma_\varphi^\ell}\right) \times \frac{1}{\sigma_{\alpha|\varphi}^\ell} \Phi\left(\frac{\alpha_i - \mu_{\alpha|\varphi}^\ell}{\sigma_{\alpha|\varphi}^\ell}\right) \quad (16)$$

where $\Phi(x) = (2\pi)^{-1/2} \exp(-x^2/2)$ denotes the standard normal distribution. The script $\ell \in \{tar, bck\}$ is used to discriminate the target and background respectively. Also, let parameter vector $\Theta_\ell = \{\mu_\alpha^\ell, \mu_\varphi^\ell, \sigma_\alpha^\ell, \sigma_\varphi^\ell, \rho_\ell\}$ be the marginal distribution parameters for region ℓ, i.e., magnitude (α)/phase (φ) mean, standard deviation, and correlation, respectively. Since the separation of two random variables in (16) is made possible by conditioning α on φ, the corresponding conditional mean and variances for amplitude can be used as [41]

$$\mu_{\alpha|\varphi}^\ell = \mu_\alpha^\ell + \frac{\rho_\ell \sigma_\alpha^\ell \left(\varphi - \mu_\varphi^\ell\right)}{\sigma_\varphi^\ell}$$

$$\sigma_{\alpha|\varphi}^\ell{}^2 = \left(\sigma_\alpha^\ell\right)^2 \left(1 - \rho_\ell^2\right). \quad (17)$$

Let $\mathbf{w} = \{w_i | i \in [1, N]\}$ be a binary window model that determines the support of the target such that $w_i = 1$ for the pixels of target and $w_i = 0$ elsewhere, and N is the total number of image pixels. Now, the image can be represented as the addition of disjoint target complex pixels (a) inside the binary window $\mathbf{w}$, and background complex pixels (b) outside the window [42], [43]. For mathematical convenience we use the one-dimensional representation of the image as $s_i = a_i w_i + b_i [1 - w_i]$.

With these notations, the problem of segmentation reduces to finding an optimal choice for **w** that maximizes the hypothesis probability $P[H_\mathbf{w}|\mathbf{s}]$, i.e., the most likely window **w**, of the target given the image data, where $H_\mathbf{w}$ represents the hypothesis that **w** is the target support. Using the Bayes rule and considering an equally likely hypothesis scenario, the maximization of *a posteriori* hypothesis probability is analogous to maximizing the conditional probability, which is expressed as the likelihood function for $H_\mathbf{w}$ as follows:

$$
\mathbf{P}(\mathbf{s}|H_\mathbf{w}, \Theta_{tar}, \Theta_{bck}) = \prod_{i=1}^{N} f_{tar}(\alpha_i, \varphi_i)^{w_i}
$$
$$
\times \prod_{i=1}^{N} f_{bck}(\alpha_i, \varphi_i)^{(1-w_i)}. \quad (18)
$$

Since no prior knowledge of the target and background is assumed, these parameters should be estimated. A maximum likelihood (ML) estimator has been utilized as follows:

$$
\widehat{\mu}_\alpha^\ell = \frac{1}{N_\ell(\mathbf{w})} \sum_{i \in \Omega_\ell} \alpha_i, \qquad \widehat{\mu}_\varphi^\ell = \frac{1}{N_\ell(\mathbf{w})} \sum_{i \in \Omega_\ell} \varphi_i
$$
$$
\widehat{\sigma}_\alpha^\ell = \left\{ \frac{1}{N_\ell(\mathbf{w})} \sum_{i \in \Omega_\ell} (\alpha_i - \mu_\alpha^\ell)^2 \right\}^{\frac{1}{2}}
$$
$$
\widehat{\sigma}_\varphi^\ell = \left\{ \frac{1}{N_\ell(\mathbf{w})} \sum_{i \in \Omega_\ell} (\varphi_i - \mu_\alpha^\ell)^2 \right\}^{\frac{1}{2}}
$$
$$
\widehat{\rho}_\ell = \frac{1}{N_\ell(\mathbf{w})\sigma_\alpha^\ell \sigma_\varphi^\ell} \sum_{i \in \Omega_\ell} (\alpha_i - \mu_\alpha^\ell)(\varphi_i - \mu_\alpha^\ell) \quad (19)
$$

where $N_\ell(\mathbf{w})$ denotes the number of pixels in the target or background window depending on script ℓ. By substituting the bivariate joint probability distribution function of (16)

into (18) and using (17) and (19), one can see that maximization of (18) is analogous to minimization of the following criterion [36]:

$$
\mathbf{J}(\mathbf{s}|H_\mathbf{w}, \Theta_{tar}, \Theta_{bck}) = N_{tar}(\mathbf{w}) \log\left(\widehat{\sigma}_\varphi^{tar} \widehat{\sigma}_\alpha^{tar} \sqrt{1 - \widehat{\rho}_{tar}^2} \right)
$$
$$
+ N_{bck}(\mathbf{w}) \log\left(\widehat{\sigma}_\varphi^{bck} \widehat{\sigma}_\alpha^{bck} \sqrt{1 - \widehat{\rho}_{bck}^2} \right). \quad (20)
$$

Optimizing criterion $\mathbf{J}(.)$ in (20) forces the snake polygon (representing $H_\mathbf{w}$) to evolve in such a way to find the statistically optimal $H_\mathbf{w}$ for the target support.

In order to carry out the optimization, a simple stochastic algorithm is employed. The idea is to model the snake by a polygon and to iteratively deform the polygon nodes in such a way that the optimization criterion in (20) decreases at every iteration. This procedure is illustrated in Fig. 6.

Several techniques such as multiresolution snake, adaptive node selection, and direction inertia are presented in [28] to increase the robustness and convergence speed of the above algorithm. The algorithm is terminated when no more contraction can be imposed on $\mathbf{J}(.)$ for long consecutive iterations.

V. 3-D IDENTIFICATION OF BIOLOGICAL MICROORGANISMS

In this section, we describe the use of Gabor wavelet transformation (GWT) to extract the feature vectors from recorded digital hologram of the biological specimen. A statistical framework is built upon the Gabor filtered digital holograms for 3-D identification of biological specimen. GWT is suitable for representing local feature vectors by providing the optimal compromise between spatial and frequency resolution. The application of Gabor wavelets has been demonstrated in a number of image processing and 2-D object recognition applications [44], [45].

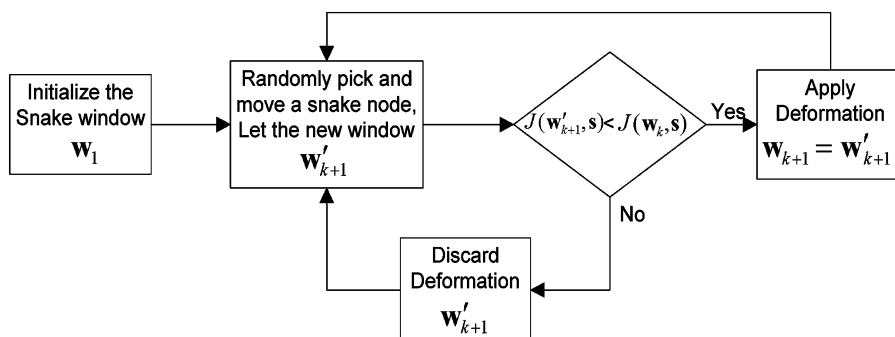There are several benefits in using space-frequency analysis when dealing with digital holograms. First, the

Fig. 6. *Schematic diagram of the primary stochastic minimization algorithm.*

interference pattern recorded at the hologram plane often contains noisy fringe patterns caused by undesirable scattering of light from the optical surface imperfections. Such noise sources will adversely affect the performance of recognition and identification of biological species. The GWT provides good noise tolerance by two mechanisms: one is due to the bandlimited behavior of the Gabor filters and the second is due to the local representation of the hologram features by the GWT coefficients. Therefore, the 3-D identification system build upon the Gabor filtered holograms is more robust to the undesirable fringe patterns. In addition, the dc component of the in-line digital hologram can be removed in the filtration process. Secondly, one can extract the feature vectors directly from the in-line digital hologram of a biological specimen. The separation between internal fringes varies with the width and thickness of the specimen and its refractive index distribution. The GWT makes it possible to determine not only the global spatial frequency response of the interference fringes but also the local features. Lastly, the Gabor wavelet transformation makes it possible to decompose the hologram into various spatial frequency components. The local fringe pattern with the selected Gabor kernel function can be obtained, and the local interference patterns of the holographic image can be consequently analyzed. The generalized 2-D Gabor elementary function is formulated as follows:

$$
\begin{aligned}
\psi(x', y') = \exp\{-&[\alpha^2(x'\cos\theta + y'\sin\theta)^2 \\
&+ \beta^2(-x'\sin\theta + y'\cos\theta)^2]\} \\
&\times \exp\{j2\pi f_0(x'\cos\theta + y'\sin\theta)\}
\end{aligned} \tag{21}
$$

where f_0 is the frequency of the sinusoid, θ is the rotation of the Gaussian and sinusoid functions, α is the sharpness of the Gaussian major axis, and β is the sharpness of the Gaussian minor axis. The continuous wavelet transformation of the 2-D in-line digital hologram $H(x', y')$ is defined by

$$
\hat{H}(x', y') = H(x', y') \otimes \psi(x', y') \tag{22}
$$

where $\otimes$ denotes convolution. We computationally reconstruct the multiscale and multiresolution sectional images of the original biological specimen at different depths along its longitudinal direction from each bandpass filtered in-line digital hologram using the inverse Fresnel transformation (IFrT) as follows:

$$
\hat{O}^S(x, y, z) = \text{IFrT}\big[\hat{H}(x', y')\big]_{z=d_0} \tag{23}
$$

where IFrT$\{\cdot\}$ denotes the inverse Fresnel transformation.

For 3-D identification of biological species, a statistical distribution-free test is employed for comparison of two populations [46]. Statistical sampling theory is useful in determining whether the difference between two observed samples is significant. For the statistical decision making, a hypothesis test can be performed by constructing the statistical sampling distribution of the test statistic. Let $X^S(1), X^S(2), X^S(3), \ldots, X^S(m)$ denote the ordered sample data set, which is randomly selected from the Sth multiscale image $\hat{O}^S$ [see (23)]. The empirical cumulative density function (ECDF) can is defined as [46]

$$
F(u) = \mathbf{P}\big(X^S(i) \le u\big) = \frac{\#\{X^S(i) \le u\}}{m}, \tag{24}
$$

where $X^S(\cdot)$ is the randomly selected pixel value in the Sth scaled image and $\#A$ is the frequency of occurrence of the event A. We define the test statistic for the null hypothesis of a reference specimen as

$$
\tilde{D} = E\left\{ \left[F_S^{ref}(u) - \hat{F}_S^{ref}(u) \right]^2 \right\} \tag{25}
$$

where $F_S^{ref}(u)$ is obtained by generating n random data samples from the Sth multiscale image. In order to obtain the sampling distribution of the test statistic, $\hat{F}_S^{ref}(u)$ is computed a number of times each with m different random samples; then the distribution of $\tilde{D}$ is calculated and used as the criterion discriminant function appropriate for the null hypothesis. The test statistic for the input data is also given by

$$
D = E\left\{ \left[F_S^{ref}(u) - F_S^{inp}(u) \right]^2 \right\}. \tag{26}
$$

To perform the hypothesis testing, a null hypothesis H_0 and alterative hypothesis H_1 are set up as follows:

$$
\begin{aligned}
H_0 &: F_S^{ref}(u) = F_S^{inp}(u) \text{ for all } u \\
H_1 &: F_S^{ref}(u) \ne F_S^{inp}(u) \text{ for at least one } u.
\end{aligned} \tag{27}
$$

Finally, the statistical p-value is computed by Monte Carlo techniques for the statistical decision to classify the specimen.

VI. 3-D TRACKING OF BIOLOGICAL MICROORGANISMS

In this section, we review a maximum *a posteriori* (MAP) region tracking algorithm derived specifically for digital

holograms to monitor/track the microorganisms in three spatial dimensions in a sequence of time-lapse holograms [29]. MAP is a powerful and well-studied point estimation method that is an extension to the ML estimator used in Section IV with an augmented a priori probability distribution. Both MAP and ML estimators use the general Bayes theorem to convert *a posteriori* probability to a computable likelihood function, which is then maximized to find an estimate to the unknown parameter.

In digital holographic microscopy, one can reconstruct the specimen volume $\mathbf{V}^{(t)}(x, y, z)$ from the digital hologram captured at time t by stacking an arbitrary number of reconstructed planes separated by distance Δz as $z_i = z_0 + i\Delta z$. Each reconstructed plane represents a complex wavefront, which conveys both magnitude and phase information from the field diffracted by the specimen. Note that $\mathbf{V}^{(t)}(x, y, z)$ is a matrix of complex numbers in which every element corresponds to the center of a specimen voxel.

Our objective is to track the subspace $\mathbf{T}^{(t)}$, representing the desired target volume in $\mathbf{V}^{(t)}(x, y, z)$. We make no assumption on the geometry or morphology of the target or how it evolves, nor do we assume a well-defined boundary between the target and background at each instant of time. However, we assume that the statistical properties of the target have small variations between two successive hologram frames. As in Section IV, we assume that the voxels are statistically independent and follow a joint bivariate Gaussian distribution for magnitude (α) and phase (φ) components, respectively, as in (16) and (17).

Consider $\mathbf{T}^{(t)} \subset \Re^3$ as the subspace occupied by the target microorganism at time t in the volume $\mathbf{V}^{(t)}$. It is possible to find the best estimate (probabilistically) of new target subspace $\hat{T}^{(t+1)}$ by maximizing the posterior probability $P(\mathbf{T}^{(t+1)} = \mathbf{T}|\mathbf{V}^{(t+1)}, \mathbf{V}^{(t)}, \mathbf{T}^{(t)})$. Thus, one can write the MAP estimate of the new target subspace $\hat{T}^{(t+1)}$ as the following:

$$\hat{T}^{(t+1)} = \arg\max_{\mathbf{T}\subset\Re^3}\left\{ P\Big(\mathbf{T}^{(t+1)} = \mathbf{T}|\mathbf{V}^{(t+1)}, \mathbf{V}^{(t)}, \mathbf{T}^{(t)}\Big)\right\}. \quad (28)$$

The posterior probability above can be interchanged with the prior probability using the Bayes rule, resulting in

$$\hat{T}^{(t+1)} = \arg\max_{\mathbf{T}\subset\Re^3}\left\{ P\Big(\mathbf{V}^{(t+1)}|\mathbf{V}^{(t)}, \mathbf{T}^{(t)}, \mathbf{T}^{(t+1)} = \mathbf{T}\Big)\right.$$
$$\left.\times P\Big(\mathbf{T}^{(t+1)} = \mathbf{T}|\mathbf{V}^{(t)}, \mathbf{T}^{(t)}\Big)\right\}. \quad (29)$$

We make minimum assumptions about the target motion in 3-D space; thus we will impose the least restrictions on the second conditional probability term. Particularly, we only assume that the target exhibits relatively smooth surfaces and may not form sharp corners. This means that the topology or

shape of next target subspace is independent of preceding frames. In mathematics words, the prior term reduces to $P(\mathbf{T}^{(t+1)} = \mathbf{T})$ [29]. It is possible to spatially localize the likelihood function in the reconstructed volume, i.e., each voxel is assigned a likelihood function by using its neighboring voxels. Assuming the complex reconstructed voxels are statistically independent, it is possible to rewrite the voxel likelihood as

$$P\Big(\mathbf{V}^{(t+1)}(\mathbf{x}_0)|\mathbf{V}^{(t)}, \mathbf{T}^{(t)}, \mathbf{T}^{(t+1)} = \mathbf{T}\Big)$$
$$= P(\mathbf{x}_0) = \prod_{\mathbf{x}\in\kappa} P_{tar}\Big[\mathbf{V}^{(t+1)}(\mathbf{x})|\mathbf{V}^{(t)}, \mathbf{T}^{(t)}\Big]^{w(\mathbf{x})}$$
$$\times \prod_{\mathbf{x}\in\kappa} P_{bck}\Big[\mathbf{V}^{(t+1)}(\mathbf{x})|\mathbf{V}^{(t)}, \mathbf{T}^{(t)}\Big]^{1-w(\mathbf{x})} \quad (30)$$

where $\mathbf{x}_0 = (x_0, y_0, z_0)$ denotes a voxel in the hologram 3-D reconstruction space and κ defines a spherical neighborhood region with radius r_0 for which $(x - x_0)^2 + (y - y_0)^2 + (z - z_0)^2 < r_0^2$. Here we have used $\mathbf{w}(.)$ as a binary volume that is one for the target voxels and zero elsewhere. We can now define the energy function as the negative log likelihood of the local spherical subregion as follows:

$$E(\mathbf{x}_0) = -\log\Big\{ P(\mathbf{x}_0) \times P(\mathbf{T}^{(t+1)} = \mathbf{T})\Big\}$$
$$= -\sum_{\mathbf{x}\in\kappa} w(\mathbf{x}) \log P_{tar}(\mathbf{x})$$
$$- \sum_{\mathbf{x}\in\kappa} (1 - w(\mathbf{x})) \log P_{bck}(\mathbf{x})$$
$$- \log P\Big(\mathbf{T}^{(t+1)} = \mathbf{T}\Big). \quad (31)$$

Using (16) and (19) on the bivariate Gaussian distribution of magnitude and phase for each voxel, (31) can be easily evaluated numerically with aid of the following expression:

$$\sum_{\mathbf{x}\in\kappa} \log P_\ell(\mathbf{x})$$
$$= N_\ell(w) \log\left(\sqrt{2\pi}\widehat{\sigma}_\varphi^\ell \widehat{\sigma}_\alpha^\ell \sqrt{1 - \widehat{\rho}_\ell^{\,2}}\right) + \frac{1}{2\left(\widehat{\sigma}_\varphi^\ell\right)^2}$$
$$\times \sum_{\mathbf{x}\in\kappa}\left(\varphi(\mathbf{x}) - \widehat{\mu}_\varphi^\ell\right)^2 + \frac{1}{2\left(\widehat{\sigma}_{\alpha|\varphi}^\ell\right)^2}$$
$$\times \sum_{\mathbf{x}\in\kappa}\left(\alpha(\mathbf{x}) - \widehat{\mu}_\alpha^\ell - \frac{\widehat{\rho}_\ell\widehat{\sigma}_\alpha^\ell\left(\varphi(\mathbf{x}) - \widehat{\mu}_\varphi^\ell\right)}{\widehat{\sigma}_\varphi^\ell}\right)^2 \quad (32)$$

in which $\ell \in \{tar, bck\}$; $N_\ell(w)$ denotes the number of voxels in $\mathbf{w}(.)$ belonging to region ℓ and the parameters

defining the bivariate distribution are sample mean μ, variance σ^2, and correlation ρ calculated from the target and background subspaces in the previous frame, as shown in (19).

In order to track the target in a 3-D space, we use a level set–based algorithm to follow the evolution of the interface between the target and the surrounding background [29]. Such an interface can be modeled in the level sets framework [29], [47], which is based on a Eulerian, initial value partial differential equation formulation as opposed to geometric methodology. Essentially, instead of explicitly treating an interface as a set of finite number of points in the space, the interface is embedded in a higher dimension function known as the level set $\phi : \Re^3 \rightarrow \Re$. In particular, assuming $\Gamma(t)$ to be the target–background interface in 3-D space at time instant t, the embedding level set is defined as $\phi(\mathbf{p}, t = 0) = \pm d$, where $\mathbf{p} = (x, y, z)$ denotes a point in $\Re^3$ space and d signifies the shortest Euclidean distance of point $\mathbf{p}$ with interface Γ. The plus and minus signs are, respectively, used for the background (exterior) and target (interior) subregions of the 3-D space. In such a formulation, the interface of interest can be explicitly written as $\Gamma(t = t_0) = \{\mathbf{p} | \phi(\mathbf{p}, t = t_0) = 0\}$, i.e., at every time instant, the interface represents the zero level set (isolevel) of the level set function $\phi(\mathbf{p}) = 0$.

The choice of level set for modeling object boundaries is primarily inspired by the similarities between the movement of such organisms and the level set evolution. On one hand, due to the highly sophisticated interaction of minute organisms with their environment, the shape, volume, orientation, and position of a microorganism can change dramatically in the course of time. On the other hand, level set formulation provides a framework in which a 3-D boundary can be embedded in a flexible balloon with simple evolution equations, which do not inherently impose any restrictions on the shape, size, or topology of the target boundary unless we choose to impose some restrictions such as smoothness. In addition, level sets provide an easy approach for targets that may split or merge. This can be a challenge in other explicit boundary representations, e.g., polygon, Fourier descriptors, splines. It has been shown in [29] that the update rule for the level set can be derived as a Hamilton–Jacobi discreet partial differential equation as

$$\phi(\mathbf{p}, t + 1) = \phi(\mathbf{p}, t) + F(\mathbf{p}) \| \vec{\nabla}_{ijk} \phi \| \qquad (33)$$

where $F(\mathbf{p})$ is the speed function at point $\mathbf{p}$ and i, j, and k are indexes spanning the 3-D spatial grid. Following (31), the speed function $F(\mathbf{p})$ is defined for each voxel based on the target versus background likelihood of the neighboring voxels in a local subspace κ and by using (32) as

$$F(\mathbf{p}) = \sum_{\mathbf{x} \in \kappa} w(\mathbf{x}) \log P_{tar}(\mathbf{x})$$
$$- \sum_{\mathbf{x} \in \kappa} (1 - w(\mathbf{x})) \log P_{bck}(\mathbf{x}) + \nabla.\left(\vec{\nabla}\phi(\mathbf{p}, t)\right) \quad (34)$$

in which the term $\nabla.(\vec{\nabla}\phi(\mathbf{p}, t))$ substitutes for $-\log P(\mathbf{T}^{(t+1)} = \mathbf{T})$ as the a priori term in (31) to essentially avoid the sharp corners (with high divergence of the level set's normal vector) to become sharper, while this term becomes negligible when the surface is flat.

The speed function in (34) derives the interface outward (in the direction of normal vector) if the target likelihood of the neighboring region is larger than the background likelihood (positive $F(\mathbf{p})$) and vice versa. Also, if the hypothetical boundary actually overlaps with the target–background interface at a certain position, $F(\mathbf{p})$ will yield zero and no movement will take place at that particular position.

VII. EXPERIMENTAL RESULTS

A. 3-D Visualization and Identification Using Digital In-Line Holographic Microscopy

In this section, we present experimental results for visualization and identification of two plant stem cell species, i.e., *sunflower* and *corn,* using in-line digital holographic microscopy, nonparametric statistical methods, and hypothesis testing. The in-line digital hologram of the stem cells is recorded with an image sensor array of 2048×2048 pixels with a pixel size of 9×9 μm^2, where the specimen is sandwiched between two 0.17 mm transparent cover slips. For magnification of biological stem cells, the microscope objective with a magnification of $60\times$ is used. The reconstruction distance between the image plane and the hologram plane is approximately 9 μm. To reconstruct the optical field in 3-D, the Fresnel transform in (3) is used to create sectional images of the stem cell digital holograms in the range of $9 \sim 10.5$ μm.

Two different samples of *sunflower* stem cell are used as training and nontraining true classes. The *corn* stem cell sample is used as the false class input in the recognition system. The real parts of sectional images of these samples are illustrated in Fig. 7.

To enhance the discrimination capability between the reference and input data sets, the Gabor wavelet filtering method is applied to the in-line digital hologram. The optimal kernel frequency of the Gabor wavelet function can be selected in such a way as to maximize the test statistic defined in (26). Fig. 8 shows the real part of *sunflower* stem cell reconstructed images from a bandpass
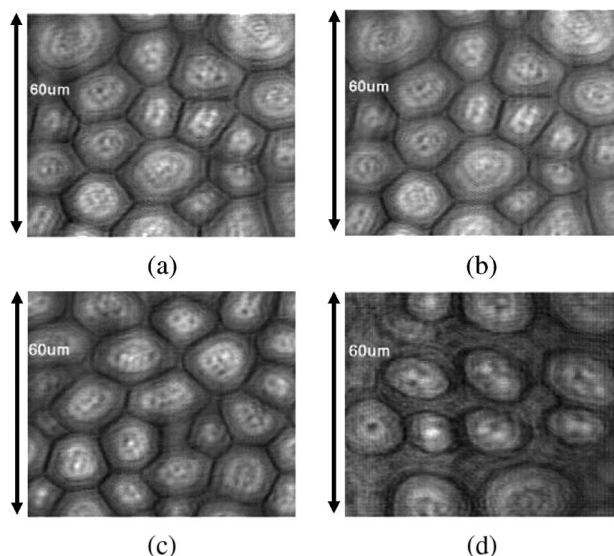
Fig. 7. *Real part of the reconstructed images from digital holograms of test samples. (a) Training true class sunflower stem cell at distance 9 μm; (b) same sample as (a) reconstructed at 10 μm; (c) nontraining true class of sunflower stem cell reconstructed at z = 9 μm; and (d) nontraining false class corn stem cell at z = 9 μm.*

filtered in-line digital hologram, where f_0 represents the Gabor kernel frequency. In the experiment, the carrier frequency of the bandpass filter was chosen in intervals of 0.005 from 0.01 to 0.50 and summed over all of the Gabor coefficients by changing the rotation angle of the Gabor kernel at intervals of $30°$ from $0°$ to $180°$ at each Gabor kernel frequency for the rotation-invariant
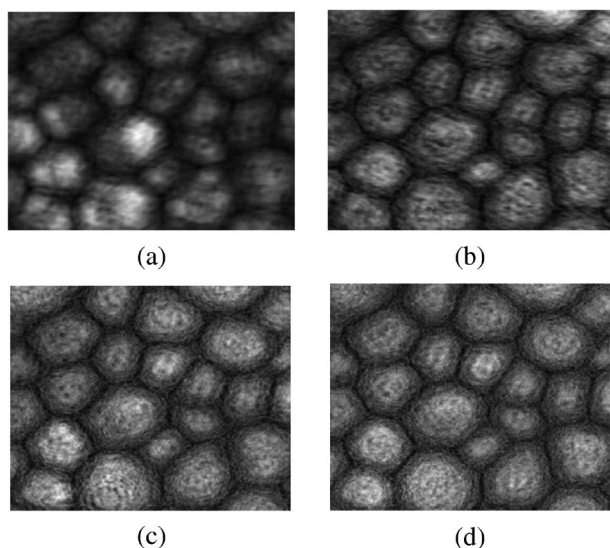
Fig. 8. *Real part of the reconstructed images (at z = 9 μm) from the feature extracted sunflower stem cell hologram using Gabor wavelet filter with f_0 = (a) 0.10, (b) 0.20, (c) 0.30, and (d) 0.40.*

property. α and β represent the sharpness of the Gaussian major axis and minor axis and are set to two and one, respectively.

For 3-D identification of the stem cells, the nonparametric statistical test for measuring the similarity between two data sets is used as described in Section V. Following (24), the reference ECDF of the reference *sunflower* stem cell, i.e., $F_S^{ref}(u)$, is computed by selecting 5000 random sample points from the hologram reconstruction at 9 μm [see Fig. 7(a)]. Also, to obtain the distribution of the test statistic $\tilde{D}$ in (25), the ECDF $\hat{F}_S^{ref}(u)$ is computed 100 times by selecting 500 random sample points at each round from the same *sunflower* sample. The process is repeated for both real and imaginary parts of the hologram reconstruction and results in the distribution of critical discriminant function $\tilde{D}$ for real and imaginary parts. Similarly, the $F_S^{inp}(u)$ is constructed by selecting 500 random sample points from the unknown input hologram. The critical discriminant function D in (26) is computed by repeating the random sampling 100 times.

Fig. 9 shows the statistical distributions of $\tilde{D}$ as the critical discriminant function for the null hypothesis and the test statistic D for the nontraining true and false classes, respectively, where the kernel frequency of the Gabor elementary function k = 0.30 is used. In this experiment, $\hat{F}_S^{ref}(u)$ and $F_S^{inp}(u)$ were generated 100 times to construct the sampling distributions of the test statistic for the null hypothesis and the test statistic for the input data, respectively. Then the central tendency of the statistical sampling distribution of the test statistic was measured.

Fig. 9(c) and (d) shows the central tendency of each statistical sampling distribution from the two different input data sets. Fig. 9 shows that the distributions of the test statistic for the true and false classes are significantly different and thus easily separable. For instance, the maximum value for test statistic $\tilde{D}$ in real part of null hypothesis is 0.0015, whereas the mean value for the same statistic in nontraining true class is 0.0012 and 0.2448 for false class, which is significantly larger. Note that the Gabor filtered digital holograms are used in experiments leading to Fig. 9. Also, note that all 100 rounds of sampling the false class data set lead to a statistic value well above the maximum value of the test statistic $\tilde{D}$ for the null hypothesis.

To show the effectiveness of GWT of digital holograms, we carry the same analysis we did above for unfiltered digital hologram.

Fig. 10 shows the distribution of test statistic for various classes including the nontraining true class (null hypothesis). As shown in Fig. 10(a), the maximum value of the test statistic $\tilde{D}$ for the null hypothesis in real part is 0.0012, whereas the mean values of the test statistic D for the real part of the nontraining true and false classes are 0.0106 and 0.0150, respectively. It is noted that the test statistic values for all 100 trials on the nontraining true and false classes
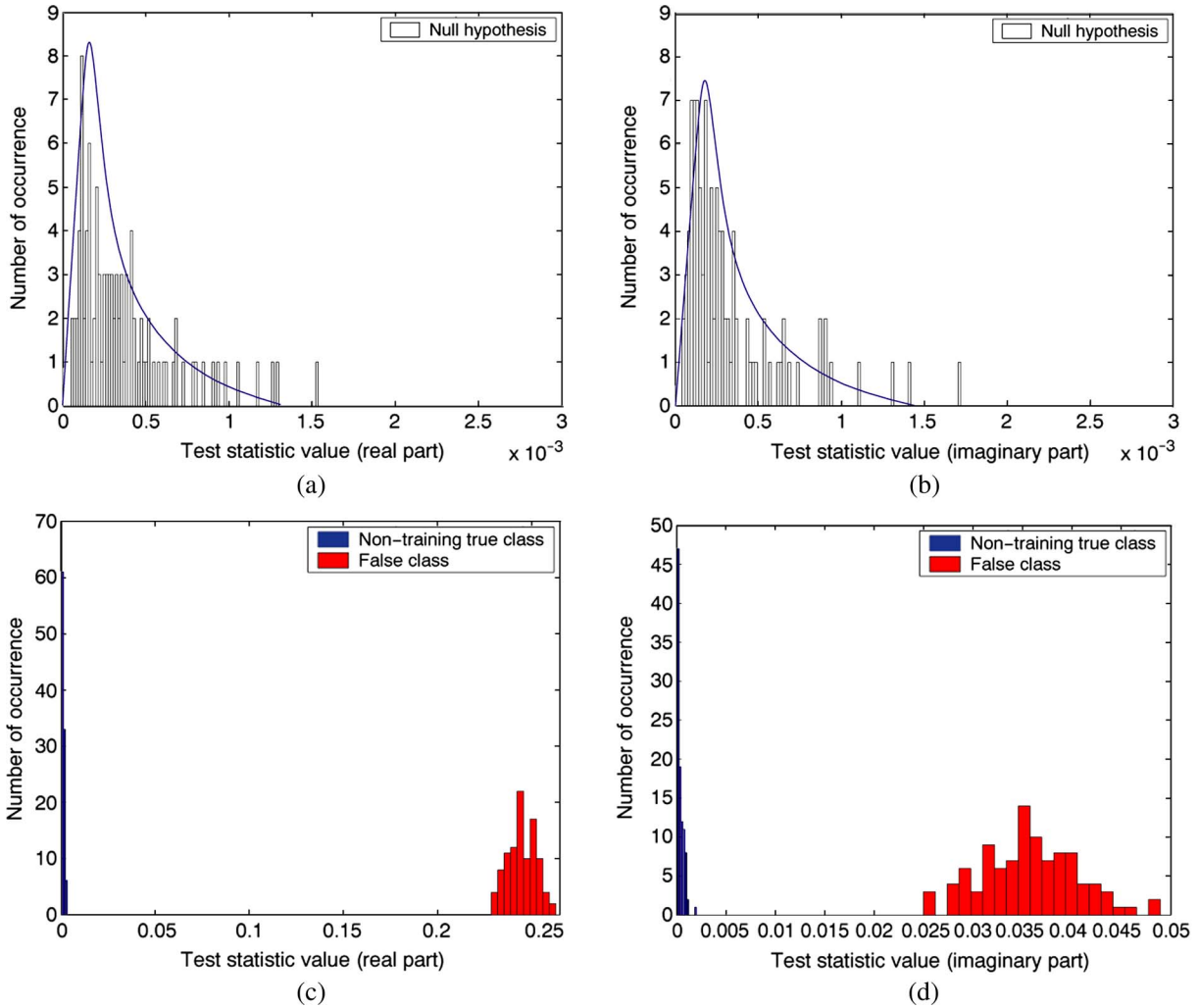
Fig. 9. *Test statistic distribution for training/nontraining true and false class stem cells from Gabor filtered digital holograms. (a), (b) Distributions of the test statistic $\tilde{D}$ for training true class (null hypothesis) in real and imaginary parts. (c), (d) Distributions of the test statistic D for unknown inputs, i.e., nontraining true and false class, in real and imaginary parts.*

are above the maximum value of the test statistic $\tilde{D}$ for the null hypothesis. It is evident in this case that it is difficult to distinguish the true and false class based on their unfiltered in-line digital holograms. This analysis shows that the discrimination performance can be increased by use of Gabor filtered in-line digital holograms.

To evaluate the performance of our 3-D identification system, a ratio is defined between the null hypothesis (true class) and the unknown input data as shown in the equation at the bottom of the page.

In order to select an optimal kernel frequency for Gabor filter, ratio R needs to be maximized. This ratio is calculated while changing the kernel frequency of the Gabor elementary function at intervals of 0.005 from 0.010 to 0.500. Fig. 11 shows the experimental results of the calculated ratio R versus the kernel frequency. As shown in Fig. 11, most of the values of R for the nontraining true class in the real and the imaginary parts are close to one, while most values of R for the false classes are greater than ten. It is noted that the optimal Gabor kernel frequency to maximize the discrimination between two stem cells is 0.275 and 0.015 in the real and the imaginary parts, respectively.

It is also evident from Fig. 11 that there are some similarities between nontraining true and false class data

$$R = \frac{\text{Averaged test statistic's value for the unknown input data}}{\text{Averaged test statistic's value for the null hypothesis}}$$
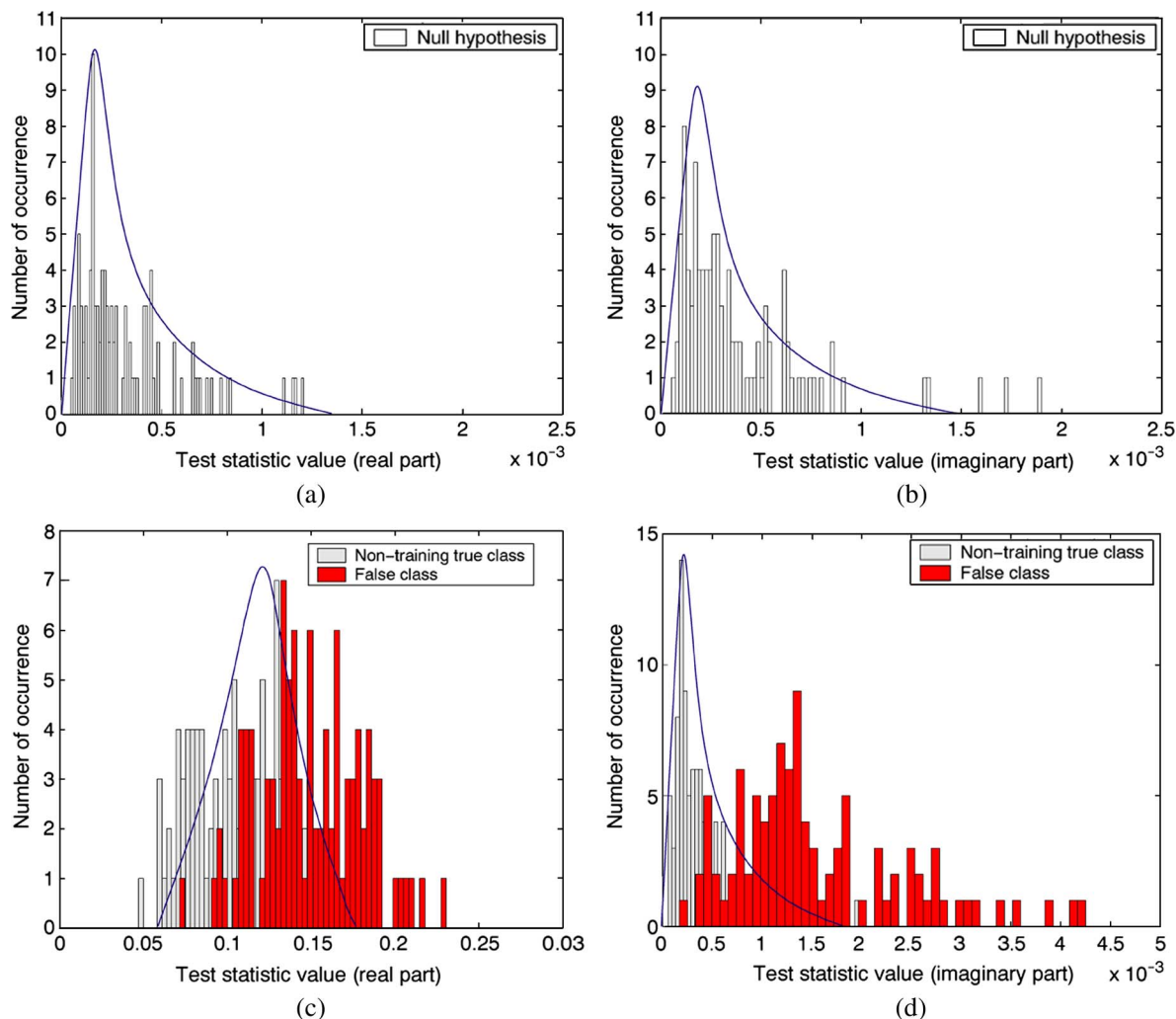
Fig. 10. *Test statistic distribution for training/nontraining true and false class stem cells from unfiltered digital holograms. (a), (b) Distributions of the test statistic D̄ for training true class (null hypothesis) in real and imaginary parts. (c), (d) Distributions of the test statistic D for unknown inputs, i.e., nontraining true and false class, in real and imaginary parts.*

in high Gabor kernel frequency ranges. We believe the reason is related to the presence of speckle noise and undesirable fringe patterns that exist in the digital holograms. The figure also shows there are some similarities between two different data sets at several low Gabor kernel frequencies. It should be also noted that the decision about classification of a sample could be based on the whole range of different Gabor kernel frequencies. Thus, the aggregated information in a frequency range (and not a single frequency) would easily discriminate between the two different species.

In order to make the final classification decision for the stem cells, the hypothesis testing based on the computed p-value is performed. Fig. 12 shows the calculated statistical p-values for different Gabor kernel frequencies, where the minimum value of the test statistic D over 100 trial data sets is used. As shown in Fig. 12, most of the p-values for the

nontraining true class are greater than 0.01 in both real and imaginary parts, while most of p-values for the false class were less than 0.01 in real and imaginary parts. The null hypothesis H_0, defined in (27), was rejected in the case where the value of the test statistic D is larger than the value of the critical discriminant function $\tilde{D}$ at the level of significance of 0.01. It is noted that the percentage of correctly matched sample data over 100 trial data sets in the real part for the true class is approximately 100% by this decision rule, while for the false class this percentage is approximately 0%. These experimental results indicate that there is a considerable similarity in the range of the Gabor kernel frequency $(0.15 < f_0 < 0.35)$ between the reference and the true class input. Thus, preliminary experimental results indicate that it may be possible to classify different species of microorganisms using the multiscale 3-D images obtained by computational reconstruction of Gabor
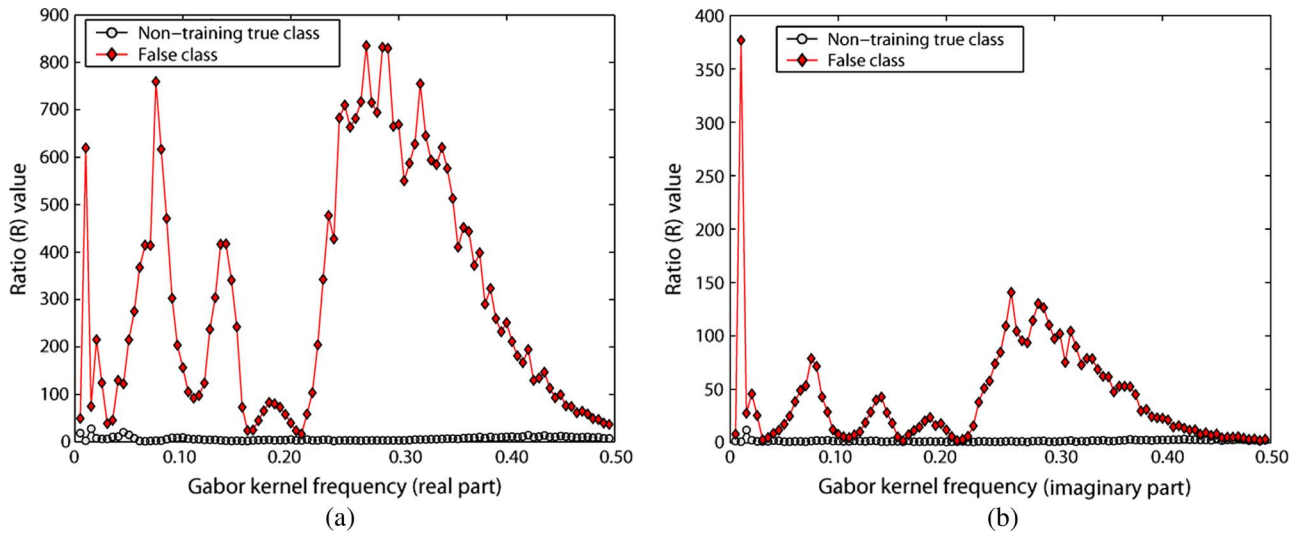
Fig. 11. *Ratio R for the nontraining true and false classes using the (a) real part and (b) imaginary part of the reconstructions from their Gabor filtered digital holograms.*

bandpass filtered in-line digital hologram and the non-parametric statistical methods.

B. 3-D Visualization by Use of Digital Holography Under Partially Coherent Light

In this section, experimental results for 3-D visualization of a sample plant stem cell using digital holographic microscopy under partially coherent illumination are presented [25]. The specimen is sandwiched between two transparent cover slips, and the exiting wavefront is magnified using a microscope objective with NA= 0.80

and $100\times$ magnification. The digital hologram of the *corn* stem cell was recorded by a 2048×2048 image sensor array with a pixel size of 9×9 μm^2. The transverse magnification at the image plane is approximately $M_t = 80\times$, and the reconstruction distance between the focus image plane and the hologram plane is approximately 25 μm.

Fig. 13(a) shows the amplitude contrast image reconstructed from the *corn* stem cell digital holograms at $z = 25$ μm using the inverse Fresnel transform described in Section II. Fig. 13(b) shows the defocused amplitude contrast image at $z = 29$ μm from the *corn* stem
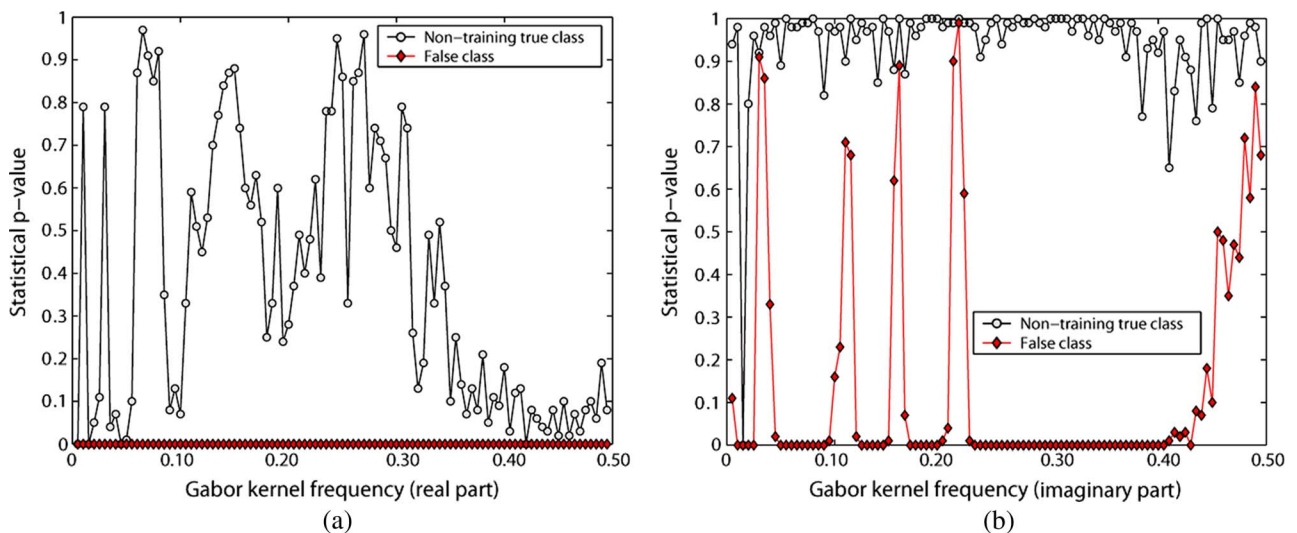
Fig. 12. *The statistical p-values between stem cells of the same class (nontraining true class) and different class (false class) using the multiscaled 3-D images using the (a) real part and (b) imaginary part of the 3-D image.*

(a)   (b)
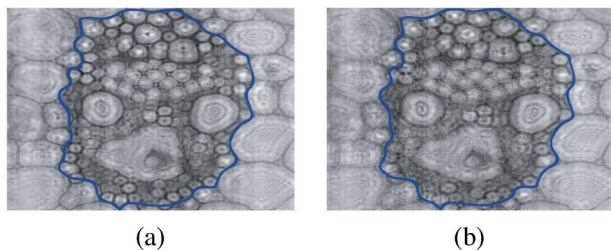
Fig. 13. *Amplitude contrast image of corn stem cell reconstructed from the partially coherent light in-line digital hologram. (a) Corn stem cell image reconstructed at the distance 25 μm. (b) Corn stem cell image reconstructed at the distance 29 μm.*

cell hologram. As shown in Fig. 13, the cell walls of *corn* stem cells are clearly reconstructed by use of partially coherent illumination in digital holography.

C. Segmentation of Biological Microorganisms

The experimental results for the segmentation using bivariate region snake technique described in Section IV are presented. Digital in-line holograms for two different species are used. An argon ion laser operates at 514.5 nm;

the CCD sensor has 2048 × 2048 pixels at 9 μm pitch, and the specimen is sandwiched between two 0.17 mm cover slips. The size of *diatom* alga is about 30–60 μm. The diffracted field is magnified by a 100×/0.8 NA microscope objective. The magnitude contrast reconstructed images are used for illustration in the figures. The snake contour is modeled as a polygon with ℓ vertexes, and the binary window function **w** is set to one inside and zero outside the polygon. The first column images in Fig. 14 show focused reconstruction planes of two different *diatom* algae over which the snakes are initialized with four nodes. Although the initial contour is completely different from target boundaries, the bivariate region snake is able to capture the microorganism body after approximately 1500 iterations [see Fig. 14(b)]. As can be seen in Fig. 14(c), the optimization traces exhibit a reasonable slope and show very slight progress after the 1500th iteration, which can be an indicator to stop the iterations.

In the next experiment, the segmentation of *sphacelaria* alga has been illustrated. This alga has a branch-like structure. The initialization captures a small portion of the organism, and throughout the iterations, the snake creeps to capture its whole body. Since the structure of algae requires many snake nodes, and the optimization

(a)   (b)   (c)
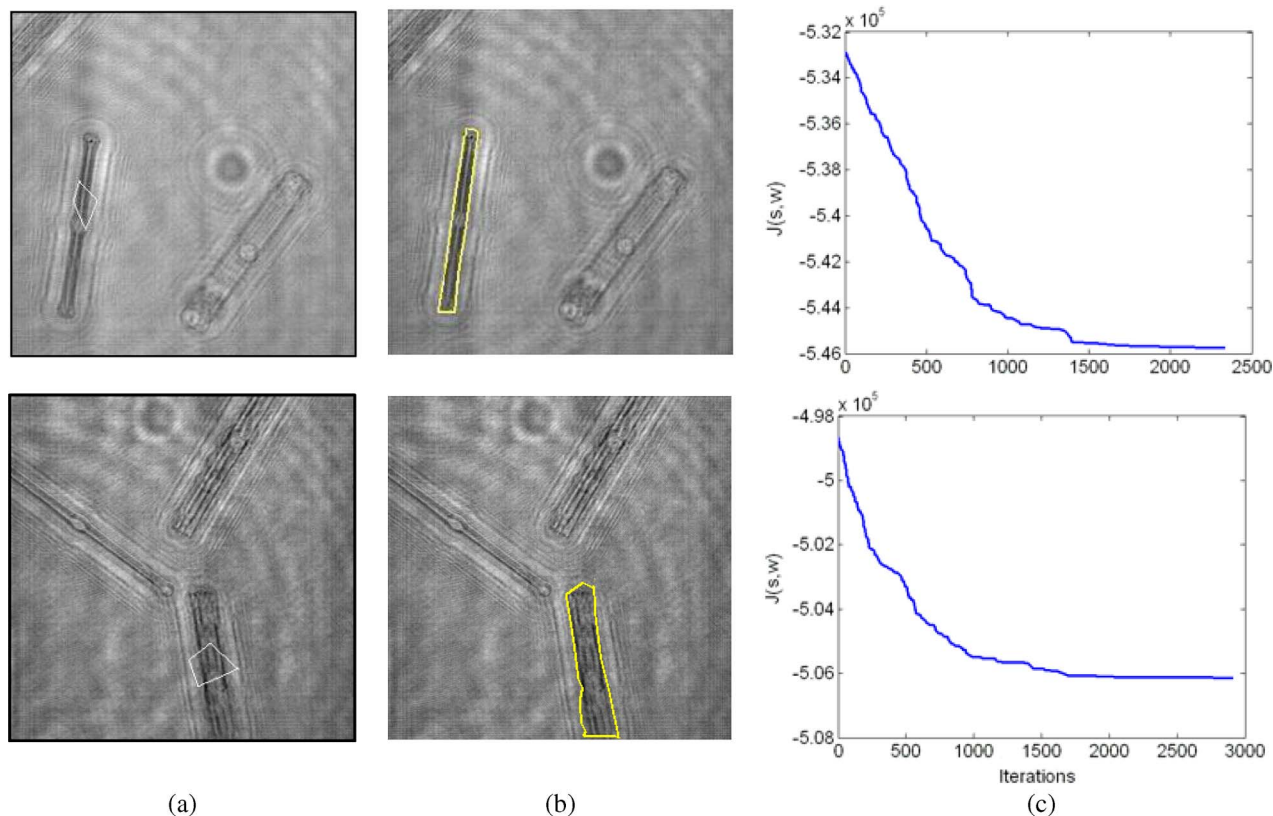
Fig. 14. *(a) Magnitude images of two diatom algae with the snake contour initialized with four points. (b) The final segmentation carried out by bivariate region snake after 1500 iterations. (c) The trace of the optimization criterion during the iterations.*
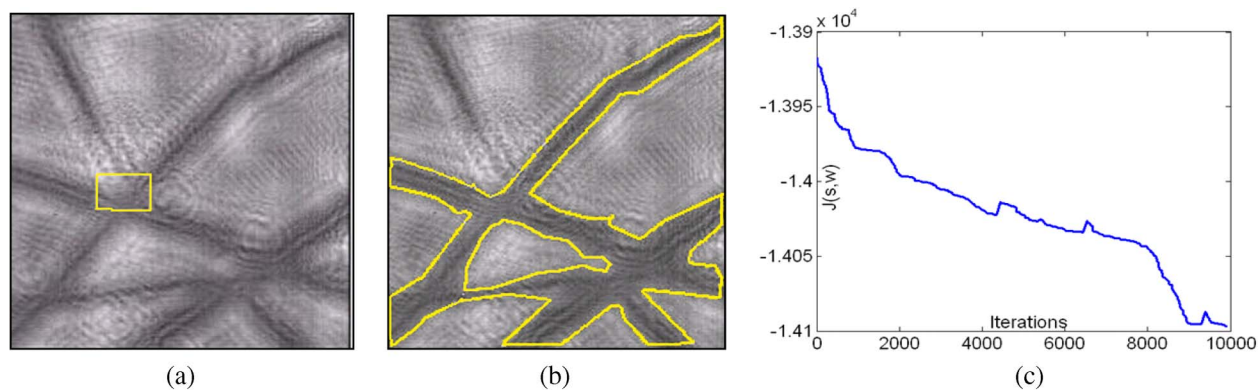
Fig. 15. *(a) Magnitude image of an out-of-focus sphacelaria alga reconstructed from a digital hologram and the five-point snake initialization. (b) The segmented microorganism. (c) The trace of the optimization criterion during the iteration. For a movie, refer to [28].*

algorithm's speed is inversely proportional to the number of snake nodes, more iteration is needed to complete the segmentation. Fig. 15(a) is intentionally reconstructed out-of-focus from a digital hologram, so it appears blurred without well-defined edges and is more challenging for segmentation. However, the bivariate region snake shows promising results in Fig. 15(b) and (c).

As the optimization algorithm is a stochastic one, the processing time depends on many parameters, like the proximity of the initial snake contour to the actual boundaries of the target, size of the digital holograms, and performance parameters in the optimization algorithm. In [28], we propose several performance boosting methods that can enhance the speed of the segmentation procedure. It takes the optimized algorithm a couple of seconds to run on a 512 × 512 pixel digital hologram in cases similar to what is shown in Fig. 14; and several seconds in cases similar to Fig. 15, in which the target boundaries are very distant from than initial snake polygon. Note that it is possible to use more sophisticated

boundary initialization algorithms to achieve an even faster segmentation.

D. Tracking of Biological Microorganisms

In this section, we present results on the MAP tracking algorithm and level set evolution described in Section VI. Among seawater algae, freshwater *diatom* algae populations are indicators of pollution, water temperature, nutrient levels, and salinity, among other things. They can also swim with their flagellum machinery. In order to simulate the motion of a microorganism, a hologram of a specimen of *diatom* algae is recorded by in-line digital holography, as described in Section II. The setup parameters are similar to Section VII-C. The magnitude and phase at the focus reconstruction plane and the volumetric reconstruction $\|\mathbf{V}\|$ for three discreet planes of a *diatom* alga is shown in Fig. 16.

A diatom is automatically segmented in the original hologram using techniques described in Section IV and computationally translated and rotated over the background
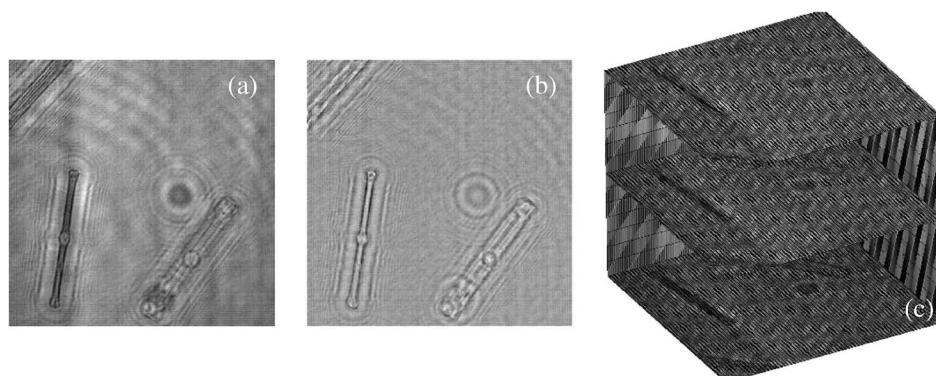
Fig. 16. *Diatom alga: (a) magnitude and (b) phase of a single plane of reconstruction in focus. (c) Three planes in the reconstruction volume.*
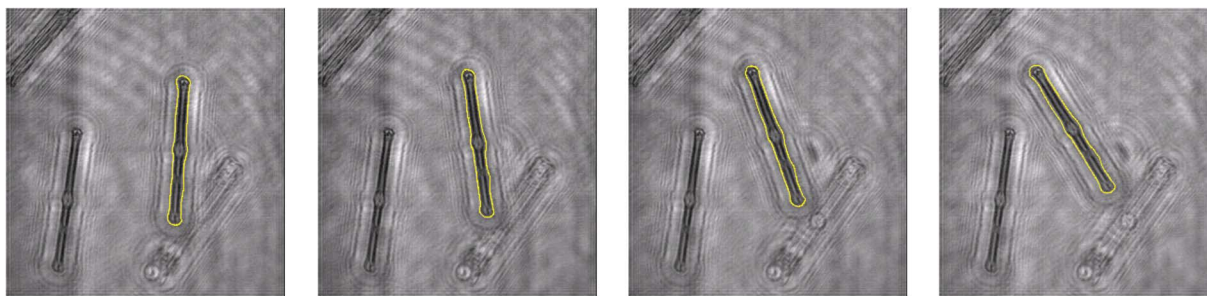
Fig. 17. *A sequence of cross-sections of the reconstructed volume from diatom algae being contoured by the isosurface (yellow line) of the 3-D tracker. For a movie, refer to [29].*

in small steps to produce 21 holograms resembling the realistic swimming of the alga in seawater. Each recorded hologram at time instant t is then reconstructed in 16 planes, all in the vicinity of the target separated by $\Delta z = 1\ \mu m$; thus the volumetric image in the form of complex data $\mathbf{V}^{(t)}(x, y, z)$ is obtained and fed into the tracking procedure. Equation (34) is calculated at each frame and used in the level set update rule (33) to achieve a new level set. A spherical neighborhood κ with $d = 20$ voxels is used.

The sequence of images in Fig. 17 shows the real part of the focused plane in reconstructed space, i.e., $\mathrm{Re}\{\mathbf{V}^{(t)}(x, y, z)\}$. The recovered target–background interface Γ is marked as a white line. This technique utilizes a stack of reconstructions for tracking; thus, even if the object of interest moves out of the best focus plane, other reconstruction planes will provide the necessary data for tracking. In addition, it has been shown that the Bayesian-based techniques do not require exact edge information; thus slightly out-of-focus organisms, which appear diffracted in the reconstruction plane, can also be tracked with a reasonable accuracy.

VIII. MULTIDIMENSIONAL IMAGING AND IDENTIFICATION OF BIOLOGICAL MICROORGANISMS

All the methods discussed so far are based on the complex amplitude of the reconstructed digital holograms of microorganisms. However, it is possible to extend these methods further to a multidimensional feature space of the microorganisms by using other degrees of freedom which are available in the optical domain, including polarization, multispectral information, and multiplexing. Polarimetric digital holography [48], [49] can be employed to add additional polarimetric information about the microorganisms' signature, which can enhance the recognition and classification. Multispectral holographic imaging and recognition [25], [50]–[52] can be used to measure the spectral response of the microorganisms and use the spectral signature in addition to the 3-D complex

amplitude for identification. Broadband light sources can be used to provide a number of wavelengths for this purpose [25]. Multiplexing techniques can be used to improve the imaging by enhancing performance metrics [34], [53], [54].

IX. CONCLUSION

In this paper, we proposed an automated, real-time optical/computational approach for sensing, visualization, identification, and monitoring of living biological specimen. In the optical sensing stage, in-line digital holographic microscopy under coherent or partially coherent illumination has been utilized. In-line digital holography is suitable for real-time 3-D sensing and visualization of dynamic events and robust to external noise factors because it requires only a single exposure. Serial sectional complex images of the 3-D volume of biological specimen can be computationally reconstructed from the single in-line digital hologram using approximations to Huygens–Fresnel integral. Also, we reviewed the conditions for which visualization with in-line digital holography is tolerant to crosstalk noise induced by the conjugate image.

Digital holographic microscopy captures information about the complex field distribution modulated by the microorganisms. Special statistical algorithms for segmentation and tracking of the individual organisms have been reviewed. These algorithms are designed with no a priori assumption about the shape, size, or mean and variance of target or background characteristics but are primarily based on an iterative approach using the joint probability distribution of the amplitude and phase of the reconstructed planes of the specimen. The segmentation algorithm enables successful segmentation of microorganisms even at a reasonable out-of-focus distance and is adaptive for any specimen shape and size. Following the same venue, the presented tracking algorithm explores maximum information of amplitude and phase content of the organism in a MAP sense. The microorganism 3-D contour was modeled as a level set that propagates in time

based on the results of the MAP estimator to simultaneously segment and track the organisms in a sequence of reconstruction volumes in time.

For 3-D identification of a biological specimen, statistical estimation and inference algorithms have been developed that allow for identification of minute specimen with simple morphology and similar thickness, size and shape. An optimal 3-D identification method has been presented using Gabor wavelet transform. In the experiments, the optimal Gabor kernel frequency, which increases the discrimination performance, was selected using the multiscale three-dimensional holographic images.

Lastly, an optical imaging system can be developed for axial-invariant 3-D identification of biological specimen based on in-line digital holographic microcopy. In addition, the system is able to detect the presence or track the position of the microorganisms in 3-D space using only a single digital hologram at each time. ∎

REFERENCES

[1] B. Javidi, *Image Recognition and Classification: Algorithms, Systems, and Applications*. New York: Marcel Dekker, 2002.

[2] I. Yamaguchi and T. Zhang, "Phase-shifting digital holography," *Opt. Lett.*, vol. 22, pp. 1268–1270, 1997.

[3] B. Javidi and F. Okano, *Three-Dimensional Television, Video, and Display Technologies*. New York: Springer-Verlag, 2002.

[4] T. Kreis, *Handbook of Holographic Interferometry*. New York: Wiley, 2005.

[5] J. W. Goodman, *Introduction to Fourier Optics* 2nd ed. Boston, MA: McGraw-Hill, 1996.

[6] F. Dubois, L. Joannes, and J.-C. Legros, "Improved three-dimensional imaging with digital holography microscope using a partial spatial coherent source," *Appl. Opt.*, vol. 38, pp. 7085–7094, 1999.

[7] D. Kim and B. Javidi, "Distortion-tolerant 3-D object recognition by using single exposure on-axis digital holography," *Opt. Express*, vol. 12, pp. 5539–5548, 2005.

[8] T. Nomura, S. Murata, E. Nitanai, and T. Numata, "Phase-shifting digital holography with a phase difference between orthogonal polarizations," *Appl. Opt.*, vol. 45, pp. 4873–4877, 2006.

[9] Y. Zhang, G. Pedrini, W. Osten, and H. J. Tiziani, "Reconstruction of in-line digital holograms from two intensity measurements," *Opt. Lett.*, vol. 29, pp. 1787–1789, 2004.

[10] G. Pedrini, W. Osten, and M. E. Gusev, "High-speed digital holographic interferometry for vibration measurement," *Appl. Opt.*, vol. 45, pp. 3456–3462, 2006.

[11] P. Ferraro, S. De Nicola, G. Coppola, A. Finizio, D. Alfieri, and G. Pierattini, "Controlling image size as a function of distance and wavelength in Fresnel-transform reconstruction of digital holograms," *Opt. Lett.*, vol. 29, pp. 854–856, 2004.

[12] S. De Nicola, A. Finizio, G. Pierattini, P. Ferraro, and D. Alfieri, "Angular spectrum method with correction of anamorphism for numerical reconstruction of digital holograms on tilted planes," *Opt. Express*, vol. 13, pp. 9935–9940, 2005.

[13] E. Cuche, F. Bevilacqua, and C. Depeursinge, "Digital holography for quantitative phase-contrast imaging," *Opt. Lett.*, vol. 24, pp. 291–293, 1999.

[14] E. Cuche, P. Marquet, and C. Depeursinge, "Spatial filtering for zero-order and twin-image elimination in digital off-axis holography," *Appl. Opt.*, vol. 39, pp. 4070–4075, 2000.

[15] M. Takeda, W. Wang, Z. Duan, and Y. Miyamoto, "Coherence holography," *Opt. Express*, vol. 13, pp. 9629–9635, 2005.

[16] A. Asundi and V. R. Singh, "Amplitude and phase analysis in digital dynamic holography," *Opt. Lett.*, vol. 31, pp. 2420–2422, 2006.

[17] B. Javidi and E. Tajahuerce, "Three dimensional object recognition using digital holography," *Opt. Lett.*, vol. 25, pp. 610–612, 2000.

[18] Y. Frauel, T. Naughton, O. Matoba, E. Tahajuerce, and B. Javidi, "Three dimensional imaging and display using computational holographic imaging," *Proc. IEEE*, vol. 94, pp. 636–654, 2006.

[19] E. Tajahuerce, O. Matoba, and B. Javidi, "Shift-invariant three dimensional object recognition by means of digital holography," *Appl. Opt.*, vol. 40, pp. 3877–3886, 2001.

[20] P. Ferraro, S. Grilli, D. Alfieri, S. D. Nicola, A. Finizio, G. Pierattini, B. Javidi, G. Coppola, and V. Striano, "Extended focused image in microscopy by digital holography," *Opt. Express*, vol. 13, pp. 6738–6749, 2005.

[21] W. Osten, T. Baumbach, and W. Juptner, "Comparative digital holography," *Opt. Lett.*, vol. 27, pp. 1764–1766, 2002.

[22] J. W. Goodman and R. W. Lawrence, "Digital image formation from electronically detected holograms," *Appl. Phys. Lett.*, vol. 11, pp. 77–79, 1967.

[23] W. Xu, M. Jericho, I. Meinertzhagen, and H. Kreuzer, "Digital in-line holography for biological applications," *Proc. Nat. Acad. Sci.*, vol. 98, pp. 11301–11305, 2001.

[24] B. Javidi, I. Moon, S. Yeom, and E. Carapezza, "Three-dimensional imaging and recognition of microorganism using single-exposure on-line (SEOL) digital holography," *Opt. Express*, vol. 13, pp. 4492–4506, 2005.

[25] I. Moon and B. Javidi, "3D visualization and identification of biological microorganisms using partially temporal incoherent light in-line computational holographic imaging," *IEEE Trans. Med. Imag.*, vol. 27, pp. 1782–1790, 2008.

[26] I. Moon and B. Javidi, "Volumetric 3D recognition of biological microorganisms using multivariate statistical method and digital holography," *J. Bio. Opt.*, vol. 11, p. 064004, 2006.

[27] I. Moon and B. Javidi, "3D identification of stem cells by computational holographic imaging," *J. Roy. Soc. Interface*, vol. 4, pp. 305–313, 2007.

[28] M. DaneshPanah and B. Javidi, "Segmentation of 3D holographic images using bivariate jointly distributed region snake," *Opt. Express*, vol. 14, pp. 5143–5153, 2006.

[29] M. DaneshPanah and B. Javidi, "Tracking biological microorganisms in sequence of 3D holographic microscopy images," *Opt. Express*, vol. 15, pp. 10761–10766, 2007.

[30] D. Gabor, "A new microscopic principle," *Nature*, vol. 161, pp. 777–778, 1948.

[31] Stern and B. Javidi, "Improved resolution digital holography using generalized sampling theorem," *J. Opt. Soc. Amer. A.*, vol. 23, pp. 1227–1235, 2006.

[32] A. Stern and B. Javidi, "Sampling in the light of Wigner distribution," *J. Opt. Soc. Amer. A*, vol. 21, pp. 360–366, 2004.

[33] L. Onural, "Signal processing issues in diffraction and holographic 3DTV," *Signal Process. Image Commun.*, vol. 22, pp. 169–177, 2007.

[34] A. Stern and B. Javidi, "Theoretical analysis of three-dimensional imaging and recognition of microorganism technique using single-exposure on-line (SEOL) digital holography," *J. Opt. Soc. Amer. A*, vol. 24, pp. 163–168, 2007.

[35] A. Lohmann, M. E. Testorf, and J. Ojeda-Castaneda, "Holography and the Wigner function," in *The Art and Science of Holography, a Tribute to Elmmett Leith and Yuri Denisyuk*, J. H. Caulfield, Ed. Bellingham, WA: SPIE Press, 2004, ch. 8, pp. 129–144.

[36] A. Stern and B. Javidi, "Space-bandwidth conditions for efficient phase-shifting digital holographic microscopy," *J. Opt. Soc. Amer. A*, vol. 25, pp. 736–741, 2008.

[37] A. Papoulis, *Systems and Transforms With Applications in Optics*. New York: McGraw-Hill, 1968.

[38] Germain and P. Refregier, "Optimal snake-based segmentation of a random luminance target on a spatially disjoint background," *Opt. Lett.*, vol. 21, pp. 1845–1847, 1996.

[39] C. Chesnaud, V. Page, and P. Refregier, "Improvement in robustness of the statistically independent region snake-based segmentation method of target-shape tracking," *Opt. Lett.*, vol. 23, pp. 488–490, 1998.

[40] M. Kass, A. Witkin, and D. Terzopoulus, "Snakes: Active contour models," *Int. J. Comput. Vision*, vol. 1, pp. 321–331, 1987.

[41] N. Mukhopadhyay, *Probability and Statistical Inference*. New York: Marcel Dekker, 2000.

[42] B. Javidi and J. Wang, "Limitations of the classic definition of the signal-to-noise ratio in matched filter based optical pattern recognition," *Appl. Opt.*, vol. 31, pp. 6826–6829, 1992.

[43] B. Javidi and J. Wang, "Optimum distortion invariant filters for detecting a noisy distorted target in background noise," *J. Opt. Soc. Amer.*, vol. 12, pp. 2604–2614, 1995.

[44] M. Lades, J. C. Vorbruggen, J. Buhmann, J. Lange, J. V. Malsburg, R. P. Wurtz, and W. Konen, "Distortion invariant object recognition in the dynamic link architecture," *IEEE Trans. Comput.*, vol. 42, pp. 300–311, 1993.

[45] T. S. Lee, "Image representation using 2D Gabor wavelets," *IEEE Trans. Pattern Anal. Machine Intell.*, vol. 18, pp. 959–971, 1996.

[46] M. Hollander and D. A. Wolfe, *Nonparametric Statistical Methods*. New York: Wiley, 1999.

[47] J. Sethian, *Level Set Methods: Evolving Interfaces in Geometry, Fluid Mechanics Computer Vision and Material Sciences*. Cambridge, MA: Cambridge Univ. Press, 1999.

[48] T. Nomura and B. Javidi, "Object recognition by use of polarimetric phase-shifting digital holography," *Opt. Lett.*, vol. 32, pp. 2146–2148, 2007.

[49] T. Nomura, B. Javidi, S. Murata, E. Nitanai, and T. Numata, "Polarization imaging of a three-dimensional object by use of on-axis phase-shifting digital holography," *Opt. Lett.*, vol. 32, pp. 481–483, 2007.

[50] P. Ferraro, S. Grilli, L. Miccio, D. Alfieri, S. De Nicola, A. Finizio, and B. Javidi, "Full color 3D imaging by digital holography and removal of chromatic aberrations," *J. Display Technol.*, vol. 4, pp. 97–100, 2008.

[51] S. Yeom, B. Javidi, P. Ferraro, D. Alfieri, S. DeNicola, and A. Finizio, "3D object sensing and recognition using multi-wavelength computational holography," *Opt. Express*, vol. 15, pp. 9394–9402, 2007.

[52] B. Javidi, P. Ferraro, S. Hong, and D. Alfieri, "3D Image fusion using multi-wavelengths digital holography," *Opt. Lett.*, vol. 30, pp. 144–146, 2005.

[53] L. Martinez and B. Javidi, "Synthetic aperture single-exposure on-axis digital holography," *Opt. Express*, vol. 16, pp. 161–169, 2008.

[54] J. Maycock, T. Naughton, B. Hennely, J. McDonald, and B. Javidi, "Three-dimensional scene reconstruction of partially occluded objects using digital holograms," *Appl. Opt.*, vol. 45, pp. 2975–2985, 2006.

ABOUT THE AUTHORS

Inkyu Moon, photograph and biography not available at the time of publication.

Mehdi Daneshpanah, photograph and biography not available at the time of publication.

Bahram Javidi (Fellow, IEEE), photograph and biography not available at the time of publication.

Adrian Stern, photograph and biography not available at the time of publication.